Star Formation
in N-Body + SPH Simulations

Ferah Munshi

A dissertation
submitted in partial fulfillment of the
requirements for the degree of

Doctor of Philosophy

University of Washington

2013

Reading Committee:

Thomas Quinn, Chair

Fabio Governato

Alyson Brooks

Program Authorized to Offer Degree:
Astronomy

University of Washington

Abstract

Star Formation
in N-Body + SPH Simulations

Ferah Munshi

Chair of the Supervisory Committee:
Professor Thomas Quinn
Astronomy

The primary focus of my thesis work is to study star formation using a series of high resolution cosmological N-body Simulations. Specifically, I have studied the total stellar-to-halo mass ratio as a function of halo mass for a new sample of simulated field galaxies using fully cosmological, LCDM, high resolution SPH + N-Body simulations carried to the present time. I find there is extremely good agreement between the simulations and predictions from the statistical Halo Occupation Distribution model presented in Moster et al. (2012). This is due to a combination of systematic factors: a) gas outflows that reduce the overall SF efficiency and b) estimating the stellar masses of simulated galaxies using artificial observations and photometric techniques similar to those used in observations. My analysis suggests that stellar mass estimates based on photometric magnitudes underestimate the contribution of old stellar populations to the total stellar mass, leading to stellar mass errors of up to 50% for individual galaxies and highlight the importance of using proper techniques to compare simulations.

Additionally, my work examines the pressure of the star-forming interstellar medium (ISM) of simulated high-resolution Milky-Way sized disk galaxies, using a kinematic decomposition of these galaxies into present-day bulge and disk components. I find that the typical pressure of the star-forming ISM in the present-day bulge is higher than that in the

present-day disk by an order of magnitude. Additionally, the pressure of the star-forming ISM in the early protogalaxy is on average, higher than ISM pressures after z = 2. This explains the why the bulge forms at higher pressures: the disk assembles at lower redshift, when the ISM is generally lower pressure and the bulge forms at higher redshift when the ISM is at higher pressures. If ISM pressure and IMF variation are tied together as suggested in studies like Conroy van Dokkum (2012), these results could indicate a time-dependent IMF in Milky-Way like systems.

Finally, my thesis work addresses the question of how well observational star formation indicators measure the true underlying star formation in dwarf galaxies. In particular, I examine Hα and the UV continuum as star formation indicators and study the timescales upon which these indicators accurately measure the underlying star formation of the galaxy. Additionally, I examine the effects of star formation prescription and resolution on applying observational indicators to simulations.

TABLE OF CONTENTS

LIST OF FIGURES

Figure Number Page

LIST OF TABLES

ACKNOWLEDGMENTS

To the Beard, Professor Thomas Quinn, who made me the scientist I am today. To Professor Fabio Governato, for giving the pushes and nudges that I needed to take this thesis to completion, in spite of all the complaining I did along the way. To the rest of my committee: Professors Julianne Dalcanton and Alyson Brooks, the strongest and most successful women that I am lucky to have as mentors.

I could imagine no other place to have completed graduate school than the University of Washington. I admire, respect and have grown very fond of all the peers that I have met through this program: they have grown to be like family and I will miss them a lot after I leave. Most notably, I will miss all the officemates I have had along the way especially those I have now, Michael Tremmel and Kristen Garofoli. And the best roommate I've ever had: Vaishali Bhardwaj, who went from my frenemy at Berkeley, to one of my best friends, and bridesmaid at my wedding.

It has been more than amazing to live in city like Seattle. I've enjoyed the food, the outdoors and found a hobby that has brought me great joy: crossfit. A giant shoutout to the wonderful and thoughtful folks I have met at the Lab. I will miss doing really hard things and throwing heavy weights around with you guys.

Last but not least, is my family. Without John and Ivan, I would not have had the motivation and support necessary to get here.

DEDICATION

To my loving husband, John
and the cutest pug in the world, Ivan
for making me feel safe and loved.

Chapter 1

INTRODUCTION

Galaxy simulations enable astronomers to track the numerous nonlinear processes that lead to a present-day galaxies. N-Body simulations provide explicit *spatially resolved* description of the physical processes involved in galaxy formation with a minimum set of assumptions. As the internal structure of galaxies holds precious clues on their assembly and subsequent evolution, the use of N-body simulations is then mandatory. Only recently have galaxy simulations been able to achieve sufficient dynamical range and physical detail to resolve the internal structure of individual galaxies. Dark matter (DM) simulations have informed our understanding of the build-up of structure in our present-day universe but in order to compare to observations, we must consider simulations that contain baryons: stars, the various types and phases of gas and their subsequent interactions, including feedback. Specifically, we need to understand how, when and where stars are forming from gas, and the effect that the evolution of stars has upon the gas content of our simulated galaxies. In this thesis I specifically explore star formation in cosmological simulations, including: how galaxies populate their dark matter halos, how the interstellar medium (ISM) structure and star formation are related in disk galaxies and observational biases in measuring star formation rates in observed galaxies.

1.1 Background Information

1.1.1 Hierarchical Galaxy Formation and Growth

On the largest scales, galaxy formation is determined by the accretion of matter into potential wells. The favored model for this process is hierarchical formation within the Λ-

Cold-Dark-Matter (LCDM) paradigm wherein small structures (halos) form first, in areas of enhanced potential, and each of these halos merge together into deeper potential wells caused by larger potential fluctuations. As time passes, structure builds from small halos to larger halos, where the larger halos are the result of mergers and growth from smaller halos.

The general picture of galaxy formation begins with an early universe relatively evenly distributed with dark and baryonic matter. Tidal torquing spins up both dark and baryonic matter into solid body rotation which both begin to collapse under the influence of gravity in overdense regions. The collapse of dissipationless dark matter is stopped by virialization; baryonic matter however, continues to collapse and decouples from the dark matter, settling into a rotating disk. This simple top-down picture is favored by many analytic models including White & Rees (1978); Fall & Efstathiou (1980); Dalcanton (1998) and can explain a variety of features of galaxies, including the Tully-Fisher relation, the Luminosity-Size relation and the mass-metalicity relation. However, these models make the basic assumptions of smooth accretion and no mergers, which is an incomplete picture.

Mergers and interactions between galaxies are an essential ingredient of galaxy formation and evolution: Toomre & Toomre (1972) was among the first to recognize that mergers can drive the evolution of galaxy types and subsequent simulations that include gas dynamics, star formation and feedback have further demonstrated that both major and minor mergers can affect the the long-term survivability of disks, bulge growth, and structural evolution of galaxies (Springel et al., 2005a).

The rate of gas cooling into halos determines its accretion into dark matter halos and its subsequent collapse into the first generation of stars. The first halos accreted pristine gas, unpolluted by metal enrichment from stellar evolution: 75% Hydrogen and the remaining in Helium (no metals). Both elements initially cooled through recombination, collisional excitation and emission, in addition to Bremsstrahlung radiation. However, at lower temperatures (less than 10^4 K), the dominant method of cooling is molecular hydrogen cooling. This low temperature cooling was the dominant cooling mechanism for forming the first generation of very massive stars (Pop III stars) in early DM halos. These are also the stars responsible for the reionization of the universe.

After the formation of the first stars, galaxy halos continue to merge and grow until they are organized into groups, clusters and field galaxies, located in filaments and surrounded by voids. The most massive potential wells house the most massive structures: galaxy groups and clusters contain giant elliptical galaxies in their centers, within a large potential well, whereas spiral galaxies and dwarfs are found in the outskirts or even in isolation. These wide variety of structures and morphological types show even greater variety when their baryon content, colors, star formation histories and metallicities are compared: Ellipticals tend to be gas poor, very red, and housing an old stellar population, while many spirals and dwarfs may be quite blue, gas rich, and still actively forming stars. Given all the variety of physics that goes into the formation and evolution of these halos (i.e., merger history, gas accretion history, star formation), the necessity and usefulness of modeling using N-body simulations becomes clear.

1.1.2 Simulations: Connecting Dark Matter and Baryons

The easiest and least computationally expensive simulations are Dark Matter (DM) only (collisionless) simulations. These simulations are incredibly vital to model halo growth as halos enter the non-linear regime. Collisionless simulations only need to model gravitational interactions, and as stated above, are thus simple, fast and inexpensive. This type of simulation has been used to study hierarchical formation of galaxies in large volumes in the context of LCDM and have been key for understanding the important aspects of galaxy formation including but not limited to: the DM halo mass function (Jenkins et al. (1998); Springel et al. (2005a); Warren et al. (2006a); Reed et al. (2007); Warren et al. (2006b); Boylan-Kolchin et al. (2009)), the mass power spectrum ((Davis et al., 1985; White et al., 1987; Jenkins et al., 1998; Springel et al., 2005a; Boylan-Kolchin et al., 2009; Teyssier et al., 2009)) and determining merger histories as a function of environment and mass (Springel et al. (2005a); Boylan-Kolchin et al. (2009); Fakhouri et al. (2010); Hopkins et al. (2009)).

Collisionless simulations have also been key in understanding DM halo substructure, DM density profiles of a given halo, and halo angular momentum as it relates to halo shape. However, collisionless simulations are limited as it has been shown that baryons do in fact have an affect on DM and vice versa.

Furthermore, in order to compare simulations to observations, we must model the baryons, which are observable, to make an 'apples-to-apples' comparison. There are many ways in which one can compare a simulation to observations, and most require comparing observations of stellar light to the stellar content in simulations. These methods include:

- N-Body + hydrodynamic simulations: fully self-consistent simulated models of galaxy formation that include gravity and gas dynamics that evolve as a function of time (see e.g., Katz (1992); Sijacki et al. (2007))

- Halo Occupation Distribution (HOD) methods & Abundance Matching methods: match observed luminosities and galaxy distributions to collisionless simulation (see e.g. Wang & White (2009); Guo et al. (2010); Moster et al. (2010)). These are discussed in detail within Chapter 2.

- Semianalytic Models: use simple equations and analytic models to describe baryonic processes for DM halos of a given mass and size (see e.g. Mo et al. (1998); Somerville et al. (2008); Guo et al. (2010)). These usually build from the outputs of a collisionless simulation.

Of the above methods, HOD methods and abundance matching have the advantage of clearly matching observations by definition but do not contain information about the systems' evolution and the physical processes that result in the observation; rather they only contain information about the system as it was at the time of the observation. Semianalytic and hydrodynamic methods have the advantage of modeling the physical processes and tracing a system's evolution but generally require a large number of free parameters that need to be tuned. Between SAMs and N-body + hydrodynamics simulations, the latter require the fewest free input parameters (knobs) and thus can explicitly trace physical processes and evolution with a minimum set of input assumptions.

There are two leading methods for implementing an N-body + hydrodynamics simulations: the lagrangian method (SPH) and the eulerian method (AMR). The former uses smoothed particle hydrodymics (SPH) and uses the equations of fluid dynamics to calculate gas temperature, pressure and density for individual particles that trace the gas. The latter uses an adaptive mesh (AMR) in which the hydrodynamic equations are solved on a grid of varied resolution, over discrete volumes. The simulations utilized and described in this thesis are SPH simulations, run using the parallel Nbody+SPH code, GASOLINE.

N-body + hydrodynamics simulations also include subgrid models for other physical processes in the galaxies, not the just gas, including but not limited to: star formation, feedback (supernovae, young stars), metal enrichment. These parameters are considered 'subgrid' as the physics of these processes may be limited by the resolution of the simulations (the size of the mesh, or the softening length in an SPH simulation). However, even with resolution limitations, hydrodynamic simulations have had vast success in reproducing observed properties of present day galaxies. For example, simulated galaxies lie on the observed scaling relations for disk galaxies as a function of time, e.g., the size – luminosity and size – velocity relations (Brooks et al. 2010), and from work presented in this thesis, the Stellar Mass-Halo Mass (SMHM) relation (Munshi et al., 2013b). The galaxies also reproduce the observed mass – metallicity relation for galaxies as a function of redshift (Brooks et al., 2007).

As stated above, the simulations in this thesis were run using GASOLINE. The following is a description of the parameters described within the GASOLINE code:

- an SPH treatment of hydrodynamics and diffusion processes
- Scaling up to several thousands of CPUs- allowing simulations to run faster and more efficiently.
- Star Formation with different IMFs, O and Fe metal enrichment.
- Gas heating from SN feedback, super-massive black holes (SMBHs) and a cosmic UV background including QSOs.

- H_2 shielding and metal line cooling; SF related to the local abundance of H_2.

1.1.3 Star Formation in the Context of the Interstellar Medium (ISM) and the Initial Mass Function (IMF)

Star formation and stellar evolution are cyclic processes: stars are born from the gas and dust that exists between stars, known as the interstellar medium (ISM) and during a star's life, depending on the star's total mass, much of that material is returned to the ISM through stellar winds and explosive events like Supernovae (feedback events). The ISM contains many components: dust in the form of silicates and polycyclic aromatic hydrocarbons (PAHs), hydrogen in the form of HI gas and also hydrogen in its molecular form: H_2. The collapse of gas into the stars begins with clouds of molecular gas (molecular clouds) which are enoromous complexes of dust and gas where temperatures are typicaly tens of kelvin and masses may reach upward of 10^6 solar masses. A cluster of star(s) begins to collapse from such a molecular cloud when the gravitational potential energy of the cloud dominates its internal energy (ie, it reaches it's Jean's length), wherein the cloud is essentially collapsing under isothermal freefall, known as homologous collapse.

$$\lambda_{Jeans} = (\frac{15k_BT}{4G\pi\mu\rho})^{0.5} \tag{1.1}$$

In the above equation, T represents cloud temperature, ρ is density of the cloud, and μ is the mean molecular weight. As the cloud collapses, the density increases, decreasing the Jean's Mass- which leads to the fragmentation of molecular clouds, forming multiple smaller collapsing cores. Collapse halts when the cores reach sufficient surface density to become optically thick. This causes the gas to heat up resulting in sufficient pressure support to stabilize the young protostar- eventually the temperatures increase enough such that fusion is sparked in the core and the protostar becomes a young stellar object and will continue it's evolution, based on its mass, along the H-R diagram. The initial mass function (IMF) gives the statistical distribution of masses of stars that form in a single star formation collapse event. Typically, the IMF is parameterized as a power law, a series of broken power laws,

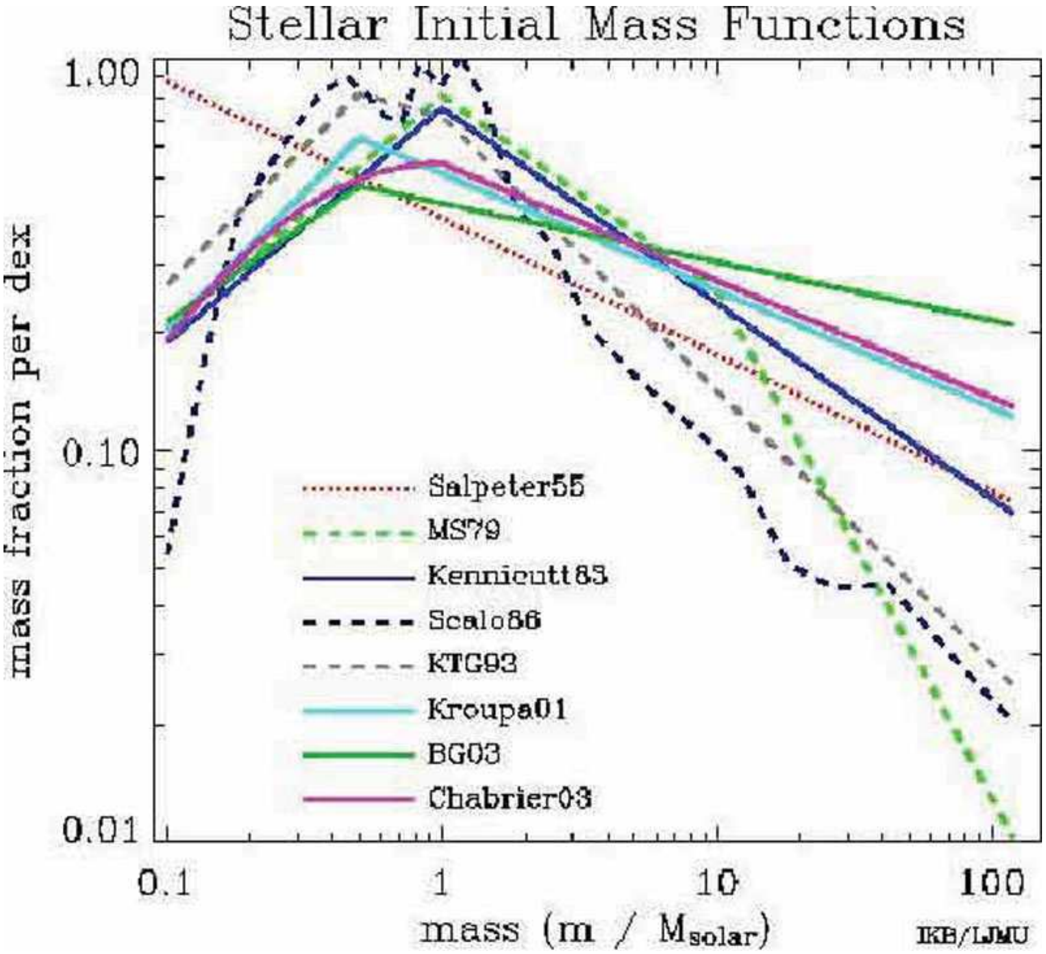

Figure 1.1 *Plot of the different functional forms of the IMF used in the literature. Figure courtesy of Ivan Baldry.*

or a log-normal distribution, in stellar mass. The IMF is crucial in interpreting the nature of galaxies because the light we observe is dominated by the highest mass stars, while the total mass in stars is dominated by the lower mass regime. If we know the IMF and the age, it is then straightforward to calculate parameters such as mass from photometry. Similarly, when looking at tracers of star formation, the IMF allows us to convert from luminosity to star formation rate. The IMF is generally assumed to be constant and universal: it does not vary within galaxies or between galaxies (Gilmore et al., 2000) and this has been shown to be the case in star clusters (see e.g. Kroupa & Weidner (2003)) and since most star formation occurs in star clusters, a universal IMF seems plausible (Lada & Lada (2003)). It is important to note, however, that PopIII stars are an exception to the universality of the IMF as ther are no observations of zero metallicity stars, indicating that all early stars must have been high mass.

The initial mass function was first derived by Ed Salpeter in 1955, where he derived a power law functional form, with α as 2.35, where m is stellar mass, and N is the number of stars:

$$dN = m^{-\alpha} dM \tag{1.2}$$

Integrating this simple form of the IMF shows us that majority of stellar mass is in low mass stars, while the luminosity is dominated by the most massive stars. One way to derive the IMF is to use field stars. To do this, first a mass function for main sequence stars is found. This mass function is then integrated over the vertical dimension of the disk. This method was first utilized by Miller & Scalo (1979). While the functional form above has much success, it is important to note that there is substantial flattening of the measured IMF at a charateristic mass of $1 M_{odot}$. Thus it is very common for the IMF to be represented by a broken power law: one to explain the low mass end and another to explain the high mass end, marked with a transition at the characteristic mass. Observations of regions of active star formation show that the IMF is set very early in the star formation process. It is unknown when exactly this mass distribution is set though there is indication that it is possibly set at the prestellar core stage from both theory and observations (Hopkins et al. (2013), Testi & Sargent (1998), Johnstone et al. (2000)). There are many mechanisms suggested as to what sets this mass distribution including: gravitational fragmentation (yields an incomplete mass spectrum), turbulence (the energy cascade with a molecular cloud sets the mass scales for collapse), gas accretion, and feedback (newly forming stars have a tremendous effect on their birth cloud via feedback processes). It is likely that it is a combination of the above processes that dictates the full spectrum of masses of the IMF. Bonnell et al. 1998 suggest that the broad peak of the characteristic mass of the IMF is set by gravitational collapse, that the high mass, Salpeter like slope is set by accretion and that at the low mass end, it is still unknown.

The origin of the stellar initial mass function (IMF) is paramount to our understanding of star formation, stellar evolution and feedback and galaxy formation. The IMF influences most of the observable properties of both stellar populations and galaxies. Detecting variations of the IMF will provide deep insights into the process by which stars form including but not limited to: the origin of the stellar mass scale, the effects of metallicity and environment and the energetics of feedback. Additionally, the IMF is a key ingredient into a huge range of models of all the above phenomena, and a necessary assumption when deriving physical parameters from observations. Despite being such a vital ingredient, the origin and variations of the IMF still remain poorly understood.

In particular, of critical importance, is the question of whether the IMF is universal or whether the IMF is sensitive to the initial conditions of star formation- i.e., the structure of the ISM in which the stars are forming (see e.g. Kroupa et al. 2011). Growing observational evidence suggests that the high mass behavior of the IMF is uniform, including observations of the IMF in the Magellanic Clouds (Bastian et al., 2010; Chabrier, 2003). However at the low mass end, there are many indications, both observationally and theoretically, that there may be a variation in the IMF. For example, Conroy & van Dokkum (2012); van Dokkum & Conroy (2011) show that the IMF in these systems is bottom heavy using gravity sensitive absorption lines in the cores of giant elliptical galaxies. This has also been independently suggested by kinematic and lensing data (Treu et al., 2010; Cappellari et al., 2012; Dutton et al., 2013). As these systems formed their stars at high redshift, these studies give us insight into the time-evolution of the IMF. Observationally, Conroy & van Dokkum (2012) show that the mass to light ratios of spheroidal systems indicate a more bottom heavy IMF at higher pressures, and at higher SFRs. This indicates that ISM pressure and the intensity of star formation are both key in understanding how and where stars form- and whether or not the IMF is varying.

1.1.3.1 Connecting Star Formation in Simulations to Observations

Galaxy stellar masses and instantaneous star formation rates (SFRs) of individual galaxies provide key information about their formation histories and comparisons betweens star formation histories (SFHs) and SFRs of different galaxy populations can clarify relationships among stellar populations. These quantities are provided directly by theoretical models and specifically by simulations, which can keep into account the complex 3-D geometries of the assembly of galaxies. However, one cannot directly observe the SFR of a galaxy; rather, it is inferred from spectra, broadband photometry (L(Hα), L(FUV)) or from resolved stellar populations (CMDs) (see e.g. Dalcanton et al. 2009). Various parts of the electromagnetic spectrum have been used to measure SFRs, including: integrated light measurements in the UV, far infrared (FIR) measurements, or nebular recombination lines. These are direct tracers of the young stellar population. All three equations that follow relating SFR to various components of the EM spectrum come from Kennicutt (1998), a review of all SFR indicators.

The ultraviolet continuum is dominated by young stars, so the SFR scales directly with luminosity. Typically, measurements are made longward of the Lyman Alpha Forest but short enough to minimize contamination from older stellar populations. The conversion between UV flux over a given wavelength is derived using population synthesis models which is dependent on calibration methods, IMF assumption, star formation timescale choice and the choice of stellar libraries. In general, it is assumed that SFR has remained constant over time scales longer than the lifetimes of the UV emitting population, and usually adopt a Salpeter IMF. The main advantages of using this method include that it is directly tied to the photospheric emission of the young stellar population and can be applied to star-forming galaxies over a wide range of redshifts. However, this method is highly sensitive to extinction and the adopted IMF. Typical extinctions can be up to 3 magnitudes (Kennicutt 1998). The equation relating SFR to the UV continuum relates the luminosity, L in the UV continuum to the SFR via a constant that is based on an assumed IMF and stellar population model:

$$SFR(M_{sun}yr^{-1}) = 1.4 \times 10^{-29} L_{\nu}(ergss^{-1}Hz^{-1}) \tag{1.3}$$

Star formation can also be measured from nebular emission: nebular lines essentially re-emit the integrated stellar luminosity of galaxies, and thus are a direct and sensitive probe of the young massive stellar population. Nebular lines include the widely used Hα line, but also include Hβ, Pα, Brα, and Brγ for example. The primary advantage of nebular emission as a star formation tracer is the high sensitivity and the direct coupling to the massive SFR. Nearby galaxies can be mapped in high resolution at these wavelengths, and Hα can be detected out to large redshift. Again, limitations include this method's sensitivity to extinction and dust, and the assumed IMF in the conversion between flux and SFR. The effects of extinction can be minimized by comparing Hα measurements with those of the IR recombination lines. The equation below relates the lineflux in the Hα line, L with the star formation rate with a coefficient that is based on an assumed IMF, dust model and stellar population library.

$$SFR(M_{sun}yr^{-1}) = 7.9 \times 10^{-41} L(H\alpha)(ergss^{-1}) \tag{1.4}$$

Finally, the far-infrared (FIR) continuum is a useful metric for the measurment of star formation within a galaxy. A significant fraction of a galaxy's bolometric luminosity is absorbed by dust and re-emited at redder wavelengths. Since the absorption cross section of dust is peaked in the FUV, the thermal infrared can be a useful, albeit, indirect tracer of star formation. Essentially, the contribution of young stars to the heating of the dust in addition to the optical depth of the dust in the star formation contribute to the FIR measurment. In the simplest case, the FIR luminosity measures the bolometric luminosity of a given starburst- which is true in dense regions like nuclear starbursts. However, in more general cases, the situation is not quite as simple: there is a contribution to the FIR from the star formation, but also other, less dense contributions, from, for example, the interstellar radiation field. For reasons such as the above, this indirect method should be used in conjunction with others, unless the case being considered is an ideal, highly starbursting case.

$$SFR(M_{sun}yr^{-1} = 4.4 \times 10^{-44} L_{FIR}(ergss^{-1}) \tag{1.5}$$

As discussed above, some indicators work better than others, and some are limited to only certain galaxy populations, or locations. For instance, using the UV continuum assumes that SF has remained constant compared to the short lifetimes of the UV population, and is very sensitive to extinction, up to 3 magnitudes (Kennicut 1998). Alternatively, Hα is highly sensitive to nebular emission from massive stars but is sensitive to IMF choice and assumes that the SFR is traced by ionized gas. Each of these indicators is likely influenced by the global environment, such as merger rate and AGN activity. It is thus important to explore the relationship between an SFR indicator and the true underlying SFR in order to appropriately calibrate these indicators using simulations. Specifically, dwarf galaxies are especially interesting environments in which to study star formation indicators: these low-mass systems are characterized by burst of star formation rather than continuous or active modes of star formation. Qualatatively, galaxies with bursty SFHs should imprint a clear signiture on the distribution of SFRs.

1.1.4 Feedback

Feedback is the process by which energy is injected back into the ISM. Without this process, star formation would be a perfectly efficient process: gas would easily cool, collapse and form stars. However, large amounts of energy from stars is, in fact, transferred back to the ISM as thermal and kinetic energy in the form of feedback, a key ingredient to any successful galaxy simulation. The injection of energy into the ISM is what regulates star formation.

When a star forms, it emits large amounts of high energy photons which starts the destruction of it's birth molecular cloud. The star evolves and travels along the main sequence, and dies a violent death, which emits lots more ionizing photons. These photons, heat, dissociate and ionize the surrounding medium in the form of supernovae and stellar winds. These feedback events also enrich the ISM by depositing metals formed in these stars, back into the ISM. The initial dump of energy from a supernova explosion results in a shock in the surrounding material, which sweeps up the nearby gas. This wave of gas may spark future star formation and also contributes to the turbulence of the ISM. Eventually, the outward expansion of the supernova slows to the speed of the surrouding turbulence, and the cloud dissipates. In short, the process of feedback regulates star formation, begining with the destruction of a star's birth cloud through to the death of the star in a violent explosion injecting energy and turbulence into the ISM. Star formation and feedback are inherently tied together not only with each other but also with the IMF which regulates how many and what types of stars form, in addition to the supernova rate.

1.1.5 Simulating the Big Picture: Putting it All Together in Simulations

The interplay between star formation, the ISM and feedback and its affects on the large scale properties of a galaxy is an incredibly difficult, detailed, and complex problem. N-body + hydrodynamic simulations are one method of studying these complex systems. By connecting gas cooling star formation and feedback we hope to trace the evolution of a galaxy, including the following processes:

- Dark Matter and gas accrete into halos, along filaments or through mergers.
- Gas cools in these halos, forms molecular clouds and star formation begins.
- The galaxy increases in mass; more stars form, evolve and explode in feedback events injecting metals and energy into the ISM. This suppresses star formation efficiency.
- Depending on the size of the halo (i.e., the depth of the potential well), supernovae and other feedback sources can expell some gas from the galaxy: most, but not all of this gas generally remains within the halo and returns to the disk after it has cooled, redistributing star formation and slowing feedback.

- While locally feedback controls star formation, globally, star formation is controlled by the accretion of gas into the galaxy and gas lost to the galaxy in stars. Up until $z = 2$, gas can be accreted rapidly into halos and builds up. Afterwards, gas mass decreases and SF decreases as well.

It is clear in this simple picture of galaxy evolution that it is imperative that simulations include prescriptions for star formation, feedback, gas accretion and gas loss. This mandates the use of baryonic physics in simulations. I have discussed techniques of following the gas in simulations, but simulations generally also include models for physical processes including star formation, supernovae feedback and metal enrichment. These recipes are generally limited by the resolution of the simulation and some of these processes, including star formation, happen on size scales smaller than the smallest resolution elements: either the grid size or smoothing length, which then must be modeled semi-analytically for that resolution element (subgrid modeling). As stated earlier, simulations have been successful in simulation the formation and evolution of galaxies over a whole hubble time and reproduce observed galaxy scaling relationships including but not limited to: the mass-metallicity relationship, the Tully-Fisher relationship and as discussed in this thesis, the stellar to halo mass relationship.

1.1.6 Limitations to Simulations and Possible Solutions

While simulations have had much success in describing the formation and evolution of galaxies, they have their share of limitations. These limitations are mainly small scale discrepancies between simulations and observations. Specifically, the traditional limitations include: the missing satellite problem (i.e., simulations predict too many small halos that are not observed), the cusp-core problem (high dark matter mass concentrations in centers of halos), and the closely related angular momentum problem (a disproportionate amount of low angular momentum material is driven to the center of halos resulting in smaller than observed disks and overly massive bulges).

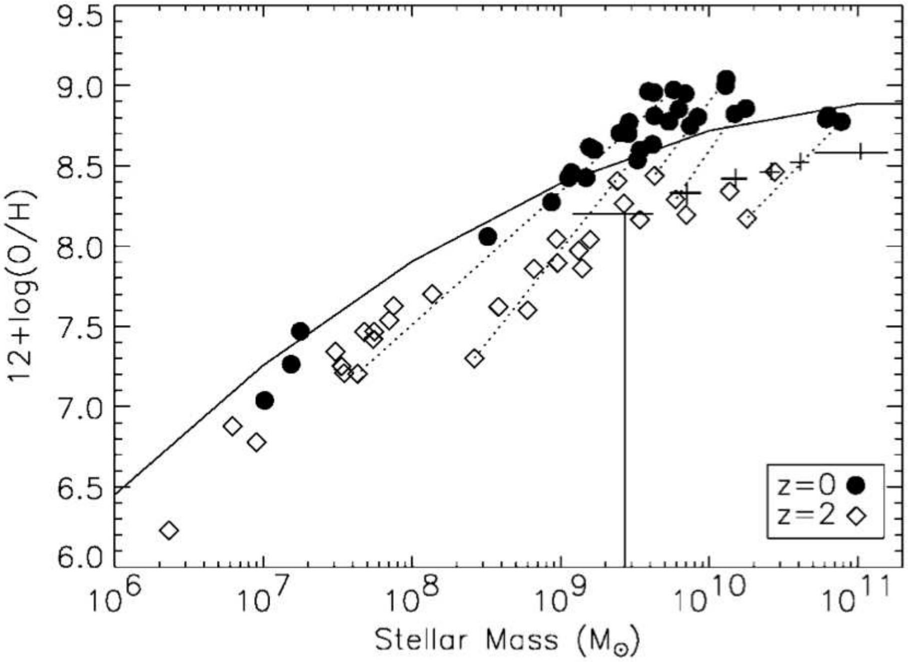

Figure 1.2 *Plot of the mass-metallicity relationship in simulations, compared with observations.* This plot shows the agreement between simulations (data points) and observations (solid line). Plot from Brooks et al. (2007).

- Missing Satellite Problem: Most notable when comparing the number of Milky-Way satellites to the number of satellites predicted by simulations of similar mass (Kaufmann, 1993; Klypin et al., 1999; Moore et al., 1999a). Even including observations of ultra faint dwarfs (see e.g. Willman et al. (2004, 2005)), a high resolution simulation will predict orders of magnitude more satellites than observed (Kuhlen et al., 2008; Springel et al., 2008; Madau et al., 2008; Boylan-Kolchin et al., 2011b,a).

- Cusp-Core Problem: When comparing the dark matter mass profiles of simulated and observed galaxies, simulations tend to have a cuspy profile while observations show evidence of cored profiles (see e.g. Moore (1994); Burkert (1995); Oh et al. (2011a)).

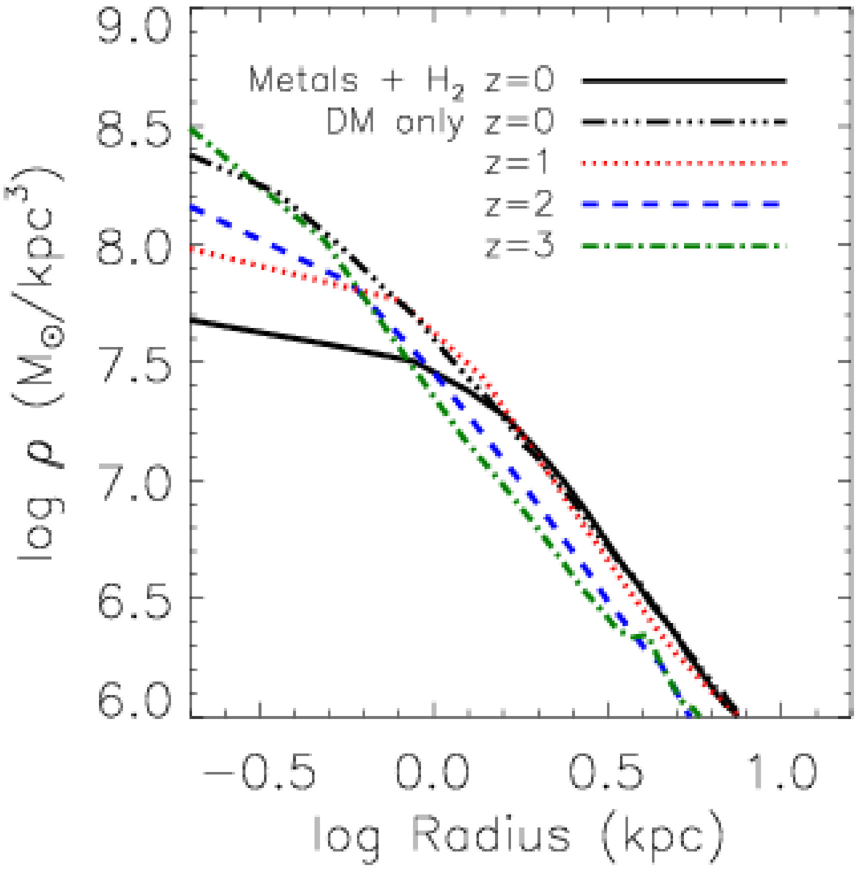

Figure 1.3 *Plot of cusp vs. core in collisionless simulations, compared with simulations that include baryons.* The black dot-dashed line shows the cuspy profile that represents the overproduction of low angular momentum DM. The inclusion of baryons and the effect of feedback shows that simulations can now reproduced cored profiles that are often observed. Plot from Governato et al. (2012).

- Angular Momentum Problem: Simulations have a decreased disk mass, and increased bulge mass (decreased high angular momentum material and increase low angular momentum material). Historically, simulations could not retain a disk because of this problem, especially during the course of mergers (Frenk et al. (1985); Bullock et al. (2001)). With the ability now to retain disks, it is bulge size that becomes the worry:

specifically bulge to disk ratios (Guedes et al., 2011; Scannapieco et al., 2010; Brooks et al., 2011).

These issues have been addressed in various ways over the years including those who advocated for a different cosmology and those who advocate for different dark matter (warm dark matter, self-interacting dark matter) over the traditional cold dark matter paradigm (Bode et al., 2001). In a less drastic vein, simulations have addressed the above issues with the addition of more extensive baryonic physics, which all focus on limiting the amount of star formation in simulations- this solves the missing satellite problem and decrease the baryonic mass within a galaxy bulge. These solutions include improved feedback methods (stronger feedback, inclusion of AGN feedback and a UV background) (Quinn et al., 1996; Gnedin, 2000; Benson et al., 2002; Somerville et al., 2008; Hopkins et al., 2011a). Increasing feedback, specifically, has been shown as an effective way to reduce the amount of low-angular momentum gas at the center of galaxies, and can even more dramatically, cause cored profiles at the centers of galaxies (through the interactions between baryons and dark matter) (Governato et al., 2010; Brook et al., 2011; Pontzen & Governato, 2012b).

1.2 Outline

This thesis broadly encompasses the complex topic of star formation, specifically in N-body+SPH cosmological simulations. Specifically this thesis tries to answer the following questions:

- How do galaxies populate their dark matter halos? What affect does feedback and baryonic physics have on the stellar to halo mass relationship?

- When and where are stars forming in galaxies? What is the structure of the ISM where these stars are forming? How does this relate to the underlying IMF of these systems?

- How well do observational star formation indicators trace star formation? What biases do we see when comparing simulations to observations? What does this tell us about the IMF in dwarf galaxies?

In Chapter 2, I describe my work comparing simulations to the observed stellar mass halo mass (SMHM) relationship. I show that using an apples-to-apples approach in comparing simulations to observations, we resolve the tension between simulations and observations. I show effect of including baryons in a simulation on the dark matter halo masses and the virial radius, as well as what happens when you apply observational mass estimates to simulations. We find that dark matter halo mass decreases by 20% between a baryonic and collisionless run, and that observations underestimate stellar mass by nearly 40%, when compared to the true underlying stellar mass distribution.

In Chapter 3, I present an analysis of the star forming ISM in the bulge and disk of 4 simulated milky way mass galaxies. I show that the pressure of the star forming ISM in the bulges of these galaxies is an order of magnitude higher than that of the star forming ISM in the disks. We suspect that this pressure differential in the ISM is evidence for a varying, time-dependent IMF which is more bottom heavy at early times, which implies a different IMF forming the stars in the bulges of these galaxies, when compared to the disk.

In Chapter 4, I once again apply observational techniques to simulations of dwarf galaxies. Specifically, I examine the percieved tension between star formation indicators in the UV and using recombination lines in Dwarf galaxies. I show that applying observational measurements to simulated dwarfs yield consistent measurements of both these star formation indicators and explore the effect of resolution on star formation in these simulations.

Finally, in Chapter 5, I present the overall conclusions of the work presented in this thesis and discuss future scientific studies based on this work, which I intend to pursue as a post-doc.

Chapter 2

REPRODUCING THE STELLAR MASS/HALO MASS RELATION IN SIMULATED ΛCDM GALAXIES: THEORY VS OBSERVATIONAL ESTIMATES

Reproduced from Munshi et al. (2013b) with permission from the AAS.

We examine the present–day total stellar-to-halo mass (SHM) ratio as a function of halo mass for a new sample of simulated field galaxies using fully cosmological, ΛCDM, high resolution SPH + N-Body simulations. These simulations include an explicit treatment of metal line cooling, dust and self-shielding, H_2 based star formation and supernova driven gas outflows. The 18 simulated halos have masses ranging from a few times 10^8 to nearly 10^{12} $M_\odot$. At z=0 our simulated galaxies have a baryon content and morphology typical of field galaxies. Over a stellar mass range of 2.2×10^3 - 4.5×10^{10} $M_\odot$ we find extremely good agreement between the SHM ratio in simulations and the present–day predictions from the statistical Abundance Matching Technique presented in Moster et al. (2012). This improvement over past simulations is due to a number systematic factors, each *decreasing* the SHM ratios: 1) gas outflows that reduce the overall SF efficiency but allow for the formation of a cold gas component 2) estimating the stellar masses of simulated galaxies using artificial observations and photometric techniques similar to those used in observations and 3) accounting for a systematic, up to 30% overestimate in total halo masses in DM-only simulations, due to the neglect of baryon loss over cosmic times. Our analysis suggests that stellar mass estimates based on photometric magnitudes can underestimate the contribution of old stellar populations to the total stellar mass, leading to stellar mass errors of up to 50% for individual galaxies. These results highlight that implementing a realistic high density threshold for SF considerably reduces the overall SF efficiency due to more effective feedback. However, we show that in order to reduce the perceived tension between the star

formation efficiency in galaxy formation models and in real galaxies, it is very important to use proper techniques to compare simulations with observations.

2.1 Introduction

In the standard Λ Cold Dark Matter (ΛCDM) paradigm (White & Rees, 1978; Fall & Efstathiou, 1980; Blumenthal et al., 1984; Dekel & Silk, 1986; White & Frenk, 1991), many galaxy properties are expected to correlate with the mass of the galaxy's host halo. In particular, the stellar-to-halo mass relation (SHM), defined as the ratio of the stellar mass (M_{star}) within a halo of total mass M_{halo} within a given over-density ($< \rho > / \rho_{crit} = 200$ in this work) is a robust estimator of the efficiency of gas cooling and star formation (SF) processes over a wide range of halo masses (Somerville & Primack, 1999; Bower et al., 2010). Both observational (Heavens et al., 2004; Zheng et al., 2007) and theoretical work (Bower et al., 2012) suggest that the SF efficiency peaks at the scale of $L^{\star}$ galaxies and declines at smaller and larger masses. On the low mass end, this decline is likely because SF is suppressed by gas heating from the UV cosmic field (Gnedin, 2000; Okamoto et al., 2008; Nickerson et al., 2011) and supernova (SN) heating with gas removal. At larger masses, energy feedback from super-massive black holes (SMBHs) is thought to be the dominant process responsible for lowering the SF efficiency (Bower et al., 2006; Croton, 2009; McCarthy et al., 2011; Johansson et al., 2012).

Recently, Moster et al. (2012, hereafter M12) and other groups (Vale & Ostriker, 2004; Conroy et al., 2006; Mandelbaum et al., 2006; More et al., 2009; Guo et al., 2010; Trujillo-Gomez et al., 2011; Behroozi et al., 2013) used the Abundance Matching Technique (AMT) and its variations (Yang et al., 2012) to derive a SHM relation of real galaxies. In its simplest form AMT assumes a monotonic relation between the stellar mass function of (real) galaxies and the underlying halo mass function. This relation is constrained by matching the observed galaxy stellar mass function to the ΛCDM halo mass function from N–body simulations. Similar works (Guo et al., 2010; Leauthaud et al., 2011, 2012) have included constraints from lensing and used slightly different underlying cosmologies. This approach has also been used to constrain the scatter in the SHM (Reddick et al., 2012) by comparing the predicted spatial clustering of DM halos (Sheth et al., 2001; Reed et al., 2007; van Daalen et al., 2012) with the observed abundances and clustering properties of galaxy populations (Blain et al., 2004; Conroy et al., 2006; Reid et al., 2010). Additionally, Behroozi et al. (2013) discuss the implications of the upturn in the faint-end slope of the stellar mass function on the SHM relationship.

Several works have highlighted how uncertainties in the derived SHM relation depend on a number of factors, some of them poorly known. For example the stellar masses of real galaxies are inferred from optical and near–IR photometric measurements and/or resolved spectra (Bell & de Jong, 2001; Kauffmann et al., 2003). This approach carries substantial uncertainties and possible degeneracies (Bell & de Jong, 2001; Bell et al., 2003; Pforr et al., 2012; Huang et al., 2012; Behroozi et al., 2010) as the observed spectral energy distribution of a galaxy is a function of many physical processes (e.g., stellar evolution, SFH and metal-enrichment history, and wavelength-dependent dust attenuation, Panter et al., 2004). Furthermore, as surveys often measure individual galaxy magnitudes within an aperture based on a surface brightness cutoff, the mass of the stellar component could be systematically underestimated by at least 20% (Graham et al., 2005; Shimasaku et al., 2001) if part of it is old (hence faint) and/or low surface brightness. Finally, the number density of galaxies will be affected by incompleteness at the faint end of the galaxy luminosity function (Dalcanton, 1998; Sawala et al., 2011; Geller et al., 2012; Santini et al., 2012). Separate from worries over the stellar mass determinations are worries about the halo mass function. While the halo mass function obtained in DM-only simulations is robustly constrained (Reed et al., 2003; Springel et al., 2005b), it has recently (Sawala et al., 2012) been shown that halo masses in DM-only simulations exceed those obtained in simulations including baryon physics by up to 30%, introducing another systematic bias in the AMT, as a galaxy of a given stellar mass is matched with a too massive halo, pushing the stellar-halo mass ratio down. Taken together, the above caveats suggest that a better understanding of the connection between galaxy masses and the underlying halo masses could in principle be gained by using realistic simulations of galaxy formation that directly include baryon physics, SF and SN feedback.

While substantial progress has been made in creating galaxies from cosmological initial conditions (Scannapieco et al., 2010; McCarthy et al., 2012; Sales et al., 2012; Stinson et al., 2012; Johansson et al., 2012), several recent studies have pointed out a large discrepancy between the SHM relation estimated for real galaxies and the one obtained in several numerical simulations of galaxy formation (Sawala et al., 2011; Guo et al., 2010). Simulations have repeatedly shown that a lack of realistic SN feedback leads to overestimating star formation as part of the general overcooling problem (Abadi et al., 2003; Governato et al., 2007; Piontek & Steinmetz, 2011; Keres et al., 2011). Most simulations that overproduce stars form galaxies that have large spheroidal components (Eke et al., 2001). Incremental improvements based on more realistic SN feedback (Thacker & Couchman, 2000; Stinson et al., 2006) led to simulations that formed galaxies with extended disks (Governato et al., 2009; Brooks et al., 2011), but still substantially overproduced stars. Only recently, a new generation of high resolution simulations demonstrated the impact of feedback at lowering SF efficiency such that SF occurs only at high gas densities (Ceverino & Klypin, 2009; Governato et al., 2010; Guedes et al., 2011; Governato et al., 2012; Zolotov et al., 2012; Brook et al., 2012). As SF is more efficient in dense gas clouds, feedback from these high density regions generate outflows that *simultaneously* improve on several long standing problems namely the substructure overabundance problem (Moore et al., 1998; Klypin et al., 1999; Benson, 2010), reducing the B/D ratio in small galaxies by removal of low angular momentum baryons (Binney et al., 2001; Governato et al., 2010; Brook et al., 2011) and forming DM cores by transferring energy from baryons to the DM (Mashchenko et al., 2006; Pasetto et al., 2010; de Souza et al., 2011; Cloet-Osselaer et al., 2012; Macciò et al., 2012; Ogiya & Mori, 2012; Pontzen & Governato, 2012a; Teyssier et al., 2012; Governato et al., 2012). Forming stars in dense gas regions is a crucial step, as observations strongly support that the spatially resolved SF is linked to the local H_2 fraction (Bigiel et al., 2008; Krumholz et al., 2009; Genzel et al., 2012), which only becomes significant at the density of star forming regions, $\geq$ 10-100 amu/cm^3.

The relationship between gas density and H_2 abundance can now be naturally implemented in simulations, and the creation and destruction of H_2 can be followed consistently (Gnedin et al., 2009; Christensen et al., 2012c), allowing much more realistic simulations to be run, and establishes a physically motivated connection between SF and high density (shielded) gas. This is indeed one of the major steps forward in the work presented here. While feedback from SNe remains still poorly understood, its effects are being observed over a large range of redshifts and galaxy masses (Martin, 1999; Wang et al., 2010). It is therefore important to evaluate a new set of high resolution simulations to test if outflows can form galaxies with realistic observational properties that also reside on the SHM relation.

Relatively less attention has been given to comparing results from simulations with observational estimates of the SHM relation in a *consistent* way. While some recent works reported (Sawala et al., 2011; Avila-Reese et al., 2011; Piontek & Steinmetz, 2011; Leitner, 2012) an excess of stars formed in simulations, they compared the galaxy stellar and total halo masses directly measured from simulations while those quantities are actually inferred from the light distribution of real galaxies. A consistent approach has been already tried with promising results in Oh et al. (2011b), where two simulated dwarfs were compared with a set of galaxies from the THINGS survey, finding that the simulations have the same central baryon and DM distribution as in the observational sample. In that work, stellar and halo masses were obtained using photometric and kinematic data for both the simulated and the real sample, finding excellent agreement (see Oh et al. (2011b) figure 5).

In this paper, we present a consistent comparison between the SHM estimated in Moster et al. (2012) and a set of high resolution simulations spanning 5 orders of magnitude in stellar masses. The evolution of galaxies is simulated at high resolution using Smoothed Particle Hydrodynamics (SPH) in a cosmological context. We focus on how galaxies populate dark matter halos ranging from $10^8 - 10^{12} M_\odot$ in a field environment and comparing results with the estimates of the SHM from M12. The four most massive, MW–like galaxies have similar resolution to the “Eris” galaxy (Guedes et al., 2011), while the smaller galaxies have even better force resolution (down to 65 pc and star particles as small as 450 M$\odot$). All simulations include the effects of metal line cooling and H_2 dependent star formation.

Our simulations include cooling, star formation, a cosmic UV background and form galaxies with structural properties comparable to the real ones. The dataset utilized is described in detail in Section 2 and has been analyzed in other papers showing that the galaxies follow the Kennicutt-Schmidt law (Christensen et al., 2012c), have cored DM profiles similar to the observed ones (Oh et al., 2011b; Governato et al., 2012) and realistic satellite populations (Zolotov et al., 2012; Brooks & Zolotov, 2012). Without any further fine tuning, in this work we compare the same simulations to the SHM relation obtained in M12, using an analysis technique comparable to the one used in the original paper to estimate their stellar and halo masses. We show that simulations form realistic galactic systems that also match the z=0 SHM of real galaxies over five orders of magnitude in stellar mass.

The paper is organized as follows: in §2 we describe the details of our N-body simulations. In §3 we compare results with the SHM predicted in M12. The results are discussed in §4.

2.2 The Simulations

The simulations used in this work were run with the N-Body + SPH code GASOLINE (Wadsley et al., 2004; Stinson et al., 2006) in a fully cosmological ΛCDM context: $\Omega_0 = 0.26$, Λ=0.74, $h = 0.73$, σ_8=0.77, n=0.96. The galaxy sample was selected from two uniform DM-only simulations of 25 and 50 Mpc per side. From these volumes a few field–like regions were selected and then resimulated at higher resolution using the 'zoomed-in' volume renormalization technique (Katz & White, 1993; Pontzen et al., 2008). This technique allows for significantly higher resolution while faithfully capturing the effect of large scale torques that deliver angular momentum to galaxy halos (Barnes & Efstathiou, 1987). With this approach, the total high resolution sample contains eighteen field galaxies, each halo resolved by 5×10^4 to a few 10^6 DM particles within R_{vir}, defined as the radius at which the average halo density = 200 × ρ_{crit}.

The force spline softening ranges between 64 and 170 pc in the high resolution regions of each volume and it is kept fixed in physical coordinates at $z < 10$. Star particles are formed with a mass of 400-8000 $M_\odot$. The halo mass range covered by the simulations spans nearly four orders of magnitude, from a few times 10^8 to 8×10^{11} $M_\odot$ (peak velocities V_{peak} = 10 to 200 km/sec), and stellar masses M_{star} from 10^4 to a few 10^{10} $M_\odot$. As other works have highlighted the importance of having a representative sample before drawing general conclusions (Brooks et al., 2011; Sales et al., 2012; McCarthy et al., 2012), the halos in our sample span a representative range of halo spin values and accretion histories (Geha et al., 2006). Galaxies and their parent halos were first identified using AHF[1] (Gill et al., 2004; Knollmann & Knebe, 2009). The total halo mass (including DM, gas and stars) is defined at a radius R_{vir}, defined as the radius at which the average halo density = $200 \times \rho_{crit}$, consistent with M12. No sub-halos have been included in our sample, although the most massive galaxies have a realistic population of satellites (Zolotov et al., 2012). More details on this dataset and the properties of the satellite population are given in Governato et al. (2012) and Brooks & Zolotov (2012).

2.2.1 H_2 fraction, Star Formation and SN Feedback

In a significant improvement, this new set of simulations include metal line cooling (Shen et al., 2010) and a dust dependent description of H_2 creation and destruction by Lyman-Werner radiation and shielding of HI and H_2 (Gnedin et al., 2009; Christensen et al., 2012c, hereafter CH12). As in CH12, the star formation rate (SFR) in our simulations is set by the local gas density and the H_2 fraction; SF $\propto (f_{H_2} \times \rho_{gas})^{1.5}$. A SF efficiency parameter, $c_* = 0.1$, gives the correct normalization of the Kennicutt-Schmidt relation (the SF efficiency for each star forming region is much lower than the implied 10%, as only a few star particles are formed before gas is disrupted by SN winds). With the inclusion of the H_2 fraction term (see also Kuhlen et al., 2011), the efficiency of SF drops to zero in warm gas with $T > 3{,}000$ K. The simulations include a scheme for turbulent mixing that redistributes heavy elements

---

[1] **A**MIGA's **H**alo **F**inder, available for download at http://popia.ft.uam.es/AHF/Download.html

among gas particles (Shen et al., 2010). With this approach, the *local* SF efficiency is linked to the local H_2 abundance, as regulated by the gas metallicity and the radiation field from young stars, without having to resort to simplified approaches based on a fixed local gas density threshold (Governato et al., 2010; Kuhlen et al., 2011). Christensen et al. (2012a) highlights the differences and improvements of H2-based star formation by comparing the total amount, distribution and history of the gas and stars formed in simulations with and without molecular hydrogen. The simulations assumed a Kroupa IMF and relative yields, but observable quantities have been converted to a Chabrier IMF, for a direct comparison with Moster et al. (2012).

As in previous works using the "blastwave" SN feedback approach (Stinson et al., 2006; Governato et al., 2012), mass, thermal energy, and metals are deposited into nearby gas when massive stars evolve into SNe. The amount of energy deposited amongst those neighbors is 10^{51} ergs per SN event. Gas cooling is then turned off until the end of the momentum-conserving phase of the SN blastwave which is set by the local gas density and temperature and by the total amount of energy injected, typically ten million years. Equilibrium rates are computed from the photoionization code Cloudy (Ferland et al., 1998a), following Shen et al. (2010). A spatially uniform, time evolving, cosmic UV background turns on at $z = 9$ and modifies the ionization and excitation state of the gas, following an updated model of Haardt & Madau (1996).

This feedback model differs compared to other "sub-grid" schemes (e.g., Springel & Hernquist, 2003; Scannapieco et al., 2012) in that it keeps gas hydrodynamically coupled while in galactic outflows. The efficient deposition of SN energy into the ISM, and the modeling of recurring SN by the Sedov solution, should be interpreted as a scheme to model the effect of energy deposited in the local ISM by *all* processes related to young stars, including UV radiation from massive stars (Hopkins et al., 2011b; Wise et al., 2012a). The SFHs of the galaxies in our simulated sample are bursty, especially those residing in halos smaller than 10^{10} $M_{\odot}$. As discussed in Brook et al. (2011) and Pontzen & Governato (2012a), a bursty SFH is necessary to remove low angular momentum baryons and create the fast outflows able to transfer energy from baryons to the DM component and create DM cores (Governato et al., 2010). These processes lead to realistic dwarf galaxies with slowly rising rotation curves and typical central surface brightnesses $21 < \mu_{B,o} < 23.5$ (Oh et al., 2011b). Outflows and the cosmic UV field progressively suppress star formation in halos with total mass smaller than a few 10^{10} . Test runs verify that the effect of energy feedback on suppressing SF is much larger than that of having a low H_2 fraction-SF efficiency (Christensen et al., 2012c).

2.2.2 Star formation efficiency as a function of galaxy halo mass

As a result of SF feedback processes, the SF efficiency is greatly reduced over the whole mass range of our simulated sample. The smallest galaxies in our sample turn only ∼0.01% of their primordial baryons into stars. The more massive galaxies in our sample turn ∼30% of their primordial baryon content into stars, but we demonstrate in the next section that using stellar masses based on photometry reduces this efficiency to an apparent 10%. Feedback expels about 70% of the gas to outside of R_{vir} in dwarf galaxies with $v_c \sim$ 40-50 km s^{-1}. Larger galaxies retain a larger fraction of their original baryons, while the smallest galaxies lose an even larger fraction of baryons due to gas heating by the cosmic UV background, which further reduces their SF (see Figure 1).

To evaluate the effect of the adopted SF model on the resulting SF efficiency of our galaxy sample, galaxies were re-simulated using the SF approach used in our older works. These reference runs adopt a lower density threshold for SF, 0.1 amu/cm^3. As discussed in several works (Governato et al., 2010; Guedes et al., 2011), a low density threshold makes SF more diffuse and locally less efficient. In this scenario, typical of low resolution simulations where star forming regions cannot be resolved, the amount of SN energy per unit mass delivered to gas particles is effectively lowered, making feedback much less effective at suppressing SF. While the galaxies in the low threshold sample have realistic disk sizes (Brooks et al., 2011) and the total amount of energy released into the gas is actually a few times larger, they contain many times more stars (see Figure 2) and overproduce stars compared to the SHM relation. The comparison between the amount of stars formed in the old and the new runs (Figure 2) demonstrates that the large decrease in the SF efficiency in the new simulations (as much as a factor of 15) is due to the improved implementation of SF in dense/H_2 rich regions (see also Governato et al., 2010). This lower SF efficiency goes a long way toward reconciling simulations of galaxy formation with current estimates of the SHM relation.

2.2.3 The Baryon Content of the Simulated Galaxies

The more massive galaxies in our sample are disk dominated, transitioning to irregular galaxies below $\sim10^{10}$ $M_\odot$. The outflows (and the UV cosmic field in halos below $\sim10^9$ $M_\odot$) significantly lower the baryon fraction of the host halos, with a strong trend of lower baryon fractions at smaller halo (stellar) mass (see Figure 1). However, because the fraction of remaining gas turned into stars is low at all galaxy masses and especially in dwarfs, the galaxies in our sample have relatively high cold gas to stellar mass ratios, typical of real galaxies over the tested range. In Figure 3 we compare the cold gas (HI) content of the simulated sample to the nearby HI surveys ALFALFA (Giovanelli et al., 2005) and SHIELD (Cannon et al., 2011). The observed dataset includes only galaxies closer than the Virgo cluster, for a better comparison with our sample of field galaxies. With the caveat that selection effects can still play a role, there is very good agreement between simulations and observations.

The HI masses are directly measured from the simulations, where HI and H_2[2] abundances are calculated on the fly. Magnitudes are measured in the SDSS r-band.

We verified that the cold gas fraction in the comparison runs adopting a low density threshold for SF is about a factor of ten lower at all halo masses. Lower resolution simulations of small mass systems have often reported the formation of relatively gas poor galaxies (Governato et al., 2007; Colín et al., 2010; Avila-Reese et al., 2011; Sawala et al., 2011). Low gas content in simulated low-z galaxies is likely due to a high efficiency of gas to stars

---

[2] note that H_2 masses are small and, while neglected in Figure 3, contribute little to the overall cold gas mass

conversion (Piontek & Steinmetz, 2011) and/or to an excessive loading factor of the SN winds.

2.3 The Stellar Mass to Halo Mass Relationship

Once individual galaxies in our sample have been identified with AHF, the Stellar Mass - Halo Mass ratio for each galaxy can then be obtained. The definition of "halo mass" includes all DM and baryons within an overdensity of 200, but not the mass associated with individual satellites (a few % of total at the most). All stars not in satellites, but within R_{200} are associated with the central galaxy in the halo. This simple approach is similar to what has been done in several previous works (Sawala et al., 2011; Brook et al., 2012) and similar to what has been used in previous comparisons between simulations and the SHM relation obtained using the AMT (Guo et al., 2010; Moster et al., 2012). Our new sample of simulated field galaxies (open circles in Figure 4) follows closely the shape and normalization of the present day SHM relation presented in M12 over the 10^9–10^{12} M$\odot$ halo mass range (solid line), with $M_{star} \propto M_{halo}^2$. This is a large improvement over most published works and confirms results on smaller samples (Governato et al., 2010; Oh et al., 2011b; Guedes et al., 2011; Brook et al., 2012) that adopted similar SF and feedback recipes.

Clearly, an approach where a) SF is limited to dense, H_2-rich gas clouds (a highly correlated situation, see Christensen et al., 2012c) and b) feedback is hydrodynamically coupled to outflows significantly reduces the SF efficiency and the present day stellar mass in galaxy sized halos over a wide mass range. Our simulations show that both a) and b) are alone not sufficient, but the combination is sufficient. We have first verified that in the absence of feedback the SF efficiency remains high even if the consumption rate of gas is long, as over the course of a Hubble time most cold gas within the galaxy eventually turns into stars. Moreover, lack of SN feedback fails to remove the low angular momentum gas, originating galaxies with an excessive spheroidal component (Governato et al., 2010; Brook et al., 2011). Similarly, if the identical SN feedback recipe used in this work is applied to simulations where SF is allowed in cold, but relatively low density gas (e.g 0.1 amu, as often adopted in the past), it fails to significantly lower the overall SF efficiency. In our sample, the mass in stars formed by $z = 0$ in galaxies with H_2/high density regulated SF is lower by as much as fifteen compared to simulations of the same halos adopting a lower density threshold. The overproduction of stars in the low threshold runs occurs *even* when metal lines cooling is neglected.

In summary, while the SF efficiency in the high threshold simulations is lower, the cold gas content is similar to that observed in real galaxies (see §2.3). Hence, a low SF efficiency was not obtained by simply increasing the feedback strength and "blowing away" all the baryons. Combined, these results show that adopting a more realistic description of *where* stars form and how feedback regulates SF leads to realistic simulations of galaxies.

However, for a meaningful comparison with observations and the SHM inferred in M12, it is important to infer *both* the stellar and halo mass from the simulations using the same techniques as the observations. This additional step is necessary as simulations directly measure the *mass distribution*, while observations infer the stellar mass from the *light distribution.* Below we show that this more accurate approach affects the results substantially. We will provide, for the first time, an accurate comparison with the present day SHM relation obtained from observational data. We used the following procedure:

- Magnitudes based on the age and metallicity of each star particle were derived using the Starburst99 stellar population synthesis models of Leitherer et al. (1999) and Vázquez & Leitherer (2005), adopting a Kroupa (2001) IMF.

- For each simulated galaxy, Petrosian aperture magnitudes (Blanton et al., 2001; Yasuda et al., 2001) were obtained in the r band. This step is necessary as observations are limited by the surface brightness of the target galaxy dropping below the sky brightness. This systematic bias underestimates the amount of light associated with individual galaxies, and it is estimated to be of the order of 20% for real galaxies (Dalcanton, 1998; Blanton et al., 2001). As our galaxies have light profiles that closely mimic those of real galaxies (Brooks et al., 2011), applying this constraint is appropriate. We verified that the amount of light lost is similar to that estimated for observational samples.

- The stellar mass of each galaxy was then estimated based on its B-V color and V total magnitude, assuming a Salpeter IMF to be consistent with adopting the same fitting formula as in Bell & de Jong (2001), namely $L_V = 10^{-(V-4.8)/2.5}$ and then $M_{star} = L_V \times 10^{-0.734+1.404\times(B-V)}$. We then utilize a conversion from Salpeter to Chabrier IMF to remain consistent with M12. We find that this procedure systematically *underestimates* the true stellar masses (by summing all star particles within R_{vir} not in satellites) of galaxies by 20-30%. This result extends over the whole range of galaxy masses. We find that the specific criteria adopted in Bell & de Jong (2001) tends to underestimate the contribution from old (i.e., high M/L) stellar populations.

- The halo mass for each simulated galaxy was measured re-running each simulation as DM–only, matching halos between the two runs and counting all mass with R_{vir} (again defined as the radius within which the average overdensity is $<\rho>= 200\rho_{crit}$). This step is necessary to follow the procedure adopted in Moster et al. (2012), where halo masses were obtained from a large cosmological simulation that did not include gas physics. This procedure avoids a subtle, but significant and systematic bias between the total halo mass measured in DM-only runs vs those of the same halos in simulations that include gas physics and feedback. In the latter simulations, feedback can remove a significant fraction of the baryons from the halo, decreasing the total mass within a fixed physical radius. The virial radius, if defined at a fixed overdensity, then shrinks, leading to a smaller total halo mass. The decrease in M_{vir} varies with mass, as it depends on the amount of baryons lost, but it can be significant, up to 30%. Since the lowest mass galaxies in our sample have lost the most baryons (in winds and UV background heating), they can experience a decrease of ∼30% in halo mass. At the high mass end, where galaxies retain most of their baryons, the simulated galaxies still see a change of 5-10% in total halo mass compared to the DM-only run (where

> obviously no baryon mass loss is possible). These results are consistent with estimates in (Sawala et al., 2012). Sawala et al. (2012) also interprets this shift as a systematic reduction in the matter infall rate. As even small amounts of baryons are removed, the gravitational attraction on surrounding material decreases, leading to a decrease in the infall rate of both gas and DM and, overtime, to a smaller halo mass. Neglecting this effect results in moving the simulations datapoints *to the left,* away from the SHM relation inferred using DM-only runs. This bias is particularly noticeable at small galaxy masses, where the SHM relation is steeper.

In Figure 4, the black solid dots show results from our simulations dataset, but using the procedure outlined above, which closely matches that adopted in M12. The normalization of the SHM is $\sim 40\%$ lower than that inferred using the simulations quantities at face value and closer overall to the SHM relation of M12. There is very good agreement between the SHM inferred from the 'artificial observations' and the fit in M12 over at least 4 orders of magnitude in halo mass. The mass of the brightest galaxies (close in mass and morphology to Milky Way analogues) goes from being higher to being slightly *lower* than the SHM. This result confirms that the "blastwave" feedback implementation is able to reduce the SF efficiency not only at small halo masses but also in present day halos around 10^{12} $M\odot$ (see also Guedes et al., 2011).

In Figure 5a we show the total halo mass ratio between the simulations that include baryons and SF vs the DM-only ones. As discussed above, halos in DM-only runs are consistently (and significantly, about 30%) more massive.In Figure 5b we show the ratio between the stellar masses obtained using a combination of Petrosian Magnitudes with Bell & de Jong (2001) M/L ratios (closely following M12) and stellar masses derived directly from the simulations. A systematic bias of about 50% is evident across the whole mass range. The results from this section highlight the importance of a careful comparison between simulations and observations. This approach further reinforces our findings that the modeling of SN feedback greatly reduces the tension between the present time SHM relation inferred from the Abundance Matching Technique for halos with total mass $<$

10^{12} M$\odot$ and the predictions from hydrodynamical simulations in a cosmological context. Without fine tuning, this better agreement also preserves the morphology of the galaxies formed, with disk-dominated massive galaxies and low mass irregulars that are gas rich. In future work, we plan to extend this approach to higher redshifts, using the appropriate criteria to measure stellar masses in high-z galaxies (e.g., Pforr et al., 2012; Maraston et al., 2012).

2.4 Conclusions

We have measured the SHM (stellar mass – halo mass) relation for a set of field galaxies simulated in a ΛCDM cosmology and compared it with the redshift zero predictions based on data from the SDSS and the Abundance Matching Technique described in M12. The comparison revealed very good agreement in normalization and shape over five orders of magnitude in stellar mass. The new simulations include an explicit description of metal lines cooling and H_2 regulated SF, and SN driven outflows. The combination of SF driven by the local efficiency of H_2 and outflows reduce the overall SF efficiency over the whole Hubble time by almost an order of magnitude compared to older simulations, with resulting $M_{star} \propto M^2_{halo}$. While a large fraction of baryons is expelled, especially in halos smaller than 10^{11} $M_{\odot}$, the resulting galaxies have an HI content comparable to those inferred by local surveys, namely ALFALFA and SHIELD. The same galaxy set has a cored central DM density distribution, similar to observations of real galaxies (Governato et al., 2012; Brooks & Zolotov, 2012).

This agreement between simulations and observational data is due to two systematic factors: 1) An implementation of SF that relates the SF efficiency to the local H_2 abundance in resolved star forming regions, resulting in localized feedback that significantly lowers the SF efficiency and 2) "observing" the simulations to properly compare them to observational estimates of the SHM relation. This approach involved creating artificial photometric light profiles of the simulated galaxies and estimating stellar masses based on aperture magnitudes. Importantly, it also requires coupling the stellar masses to halo masses derived from DM-only simulations, rather than the baryonic simulations. Our analysis shows that adopting photometric stellar masses contributes to a 20-30% *systematic* reduction in the estimated stellar masses. Stellar mass estimates based on one band photometric magnitudes are likely to underestimate the contribution of old stellar populations (reflecting the larger contribution to the total flux coming from younger stars). This systematic effect is further exacerbated by the use of aperture based magnitudes, adding another 20-30% due to neglecting the contribution of low surface brightness populations. Finally, a third systematic effect comes from a difference in halo masses in collisionless (DM-only) simulations vs simulations including baryon physics and outflows. Baryon mass loss makes halo masses smaller by up to 30% when calculated at the same overdensity (200 in our paper and M12). The effect of removing these biases is to move the simulation points in Figure 4 further lower and to the right, closer to the SHM.

Notwithstanding the improvements described in this and other recent works, further adjustment to our numerical schemes to model SF and feedback processes are most likely required, as more observational constraints become available and our understanding of SF improves. In future work we plan to extend our analysis of the stellar mass – halo mass relation to higher redshifts and larger galaxy masses. The results presented in M12 point to a possible discrepancy between the shape of the star formation history of real galaxies vs the simulated ones. Given the difficulty to obtain robust estimates from faint and distant galaxy samples, we expect that the approach outlined in this work, i.e. creating artificial observations to more directly compare simulations with observations, will play an important role.

2.5 Supplemental Analysis

In this section I present extra analysis not included in the published paper regarding the stellar mass to halo mass relation in our simulations. Specifically, I compare our abundance matching results to the results from Behroozi (2010). Note that the Behroozi results show an upturn in the SHM relationship toward lower masses: this is due to the fact that this analysis includes corrections for incompleteness in the faint end of the luminosity function, and adjusts the matching between the halo mass function and the luminosity function to adjust for small galaxies missed by surveys. We also examine the affect of baryons on dark matter halos by comparing virial radii and virial masses of runs completed with baryons and those that are collisionless. In figures 2.8 and 2.9, we verify that for our galaxies with halo masses greater than 10^{10} $M\odot$ that the change in halo mass can be explained entirely by a change in virial radius that results from a new overdensity after baryons are lost. In halos smaller than this, the smaller virial radius in the SPH run cannot completely account for the change in halo mass, and it appears that the lowered mass of these halos also leads to lower accretion. We also compared the DM mass between a baryonic and collisionless run and we can see that the DM mass within the same radius is the same in each run for halos more massive than 10^{10} solar masses. In these more massive galaxies, the change in the halo mass can be entirely accounted for by the change in virial radius. In the lower masses, there's some indication that a small fraction of DM really isn't within the same radius, and that there might be a lowered accretion rate in these halos. In comparing the virial radii, we compared total mass. For the SPH runs, we added back in the baryonic mass that had been lost. The results are consistent with the DM mass plot, where the larger halos are explained entirely due to the change in virial radius, and lower mass halos indicating some small change in accretion within that radius.

In Figure 2.11, we also show that as halo mass increases, star formation efficiency increases by examining as a function of halo mass, the ratio of stellar mass to halo mass. Note that low mass galaxies are very inefficient at forming stars, and that as halo mass increases, star formation efficiency increases. Additionally, we also examine the efficacy of using M/L ratios to estimate stellar mass in Figure 2.10. I created "images" of the galaxy that contain different portions of the stellar mass of the galaxy: each image (at each formation time point) contains newer and newer stars, i.e., as the points increase along the Tform axis, they contain and increasing amount of younger stellar population. For each image that I generated, I measured the stellar mass, directly from the simulation (actual) and stellar mass measured by using mass to light ratios (measured). The ratio of the two quantities tells us what amount of the total stellar mass is recovered by using M/L ratios (using B-V color) to estimate mass, for a given stellar population. As we include younger stellar populations, we note that the mass recovered by stellar populations becomes better which implies that using M/L ratios to estimate stellar mass is an underestimate as it does not recover the old stellar population.

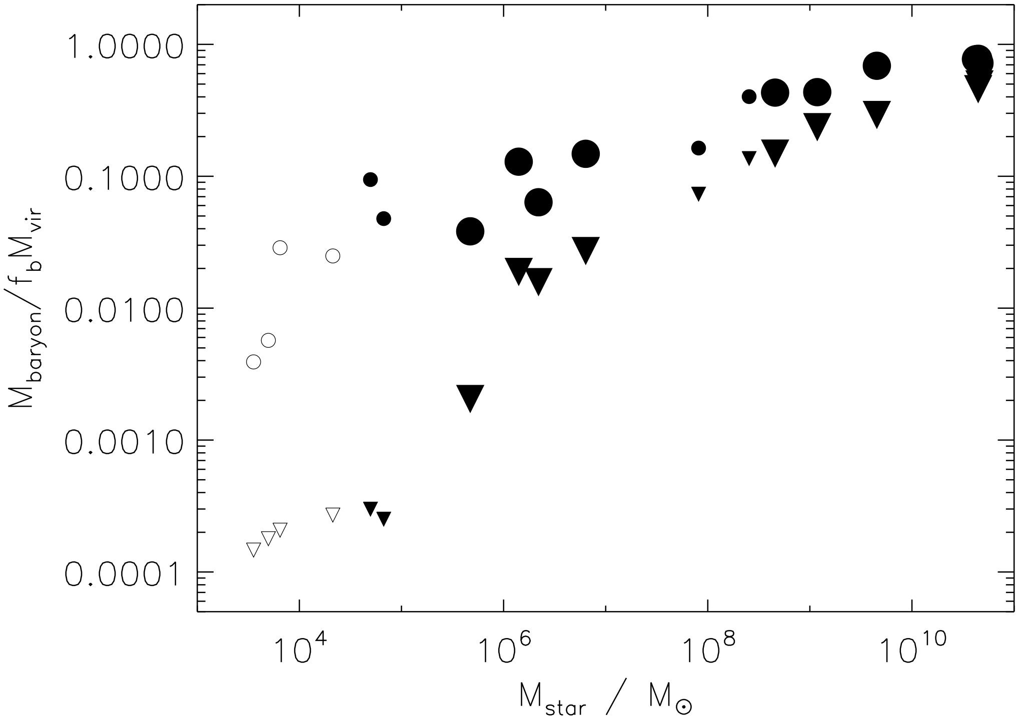

Figure 2.1 *Baryonic fraction with respect to the cosmic ratio, for simulated field galaxies as a function of stellar mass, measured at z=0.* Circles are the "direct from simulation" results, including all gas and stars within R_{200}. Triangles are the "observable" baryon fractions, includind all stars and all the 'observable' cold gas (defined as 1.4 × (HI+H2), within R_{200}). The empty symbols are galaxies with no observable gas (cold gas mass < 100 $M_\odot$). Symbol sizes represent the different mass resolutions of galaxies in the sample. Smaller symbols are the higher mass resolution by a factor of 8 when compared to the larger symbols. Galaxies below 10^8 $M_\odot$ lose a significant fraction of baryons due to heating from the cosmic UV background and SN feedback.

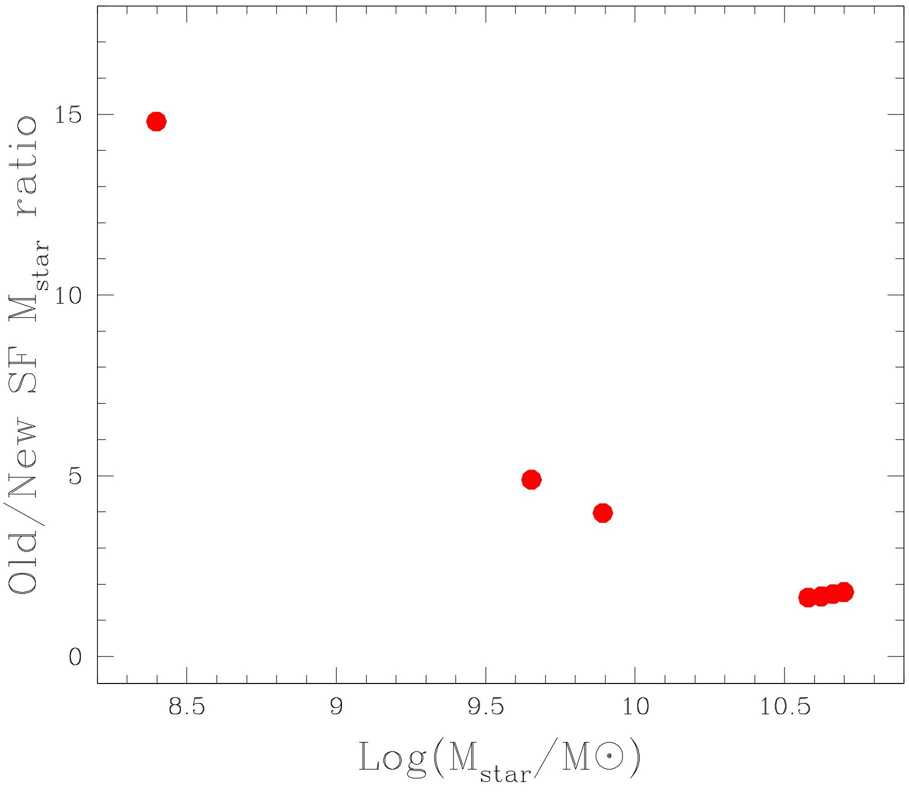

Figure 2.2 *The stellar mass ratio between the galaxies simulated with the old 'low density SF threshold' and the new sample.* In the new sample SF is regulated by the local abundance of molecular hydrogen, resulting in feedback significantly lowering the total SF efficiency. All quantities as measured directly from the simulations.

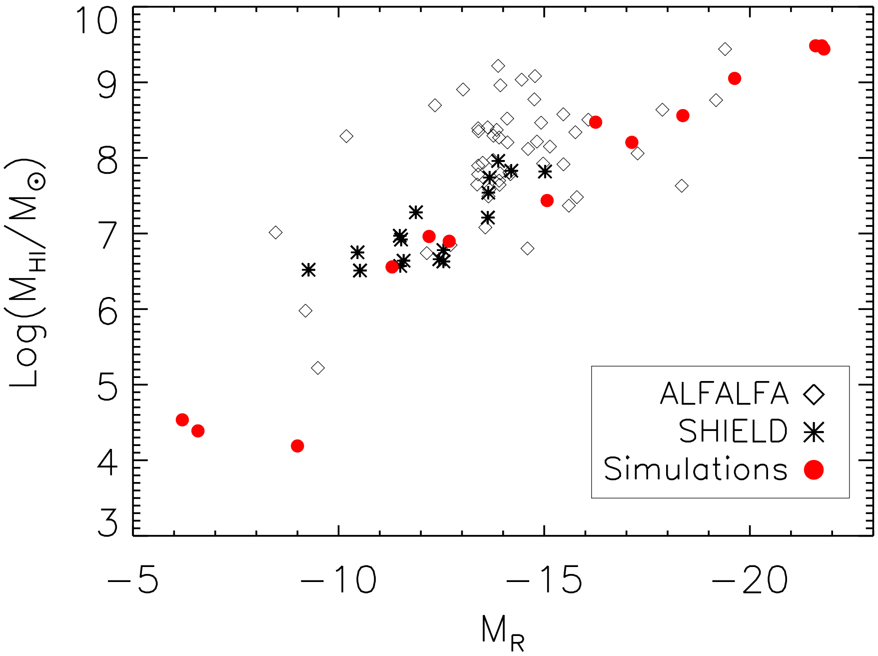

Figure 2.3 *The cold gas mass as a function of stellar mass. Simulations vs. SHIELD and ALFALFA data.* The HI mass of each galaxy in the simulated sample is plotted vs the SDSS *r*-band magnitude and compared to two samples from nearby surveys. Red solid dots: simulations. Diamonds: ALFALFA survey. Asterisks: SHIELD survey. While feedback removes a large fraction of the primordial baryons, the simulated galaxies have a high gas/stellar mass ratio, comparable to the observed samples. Most of the cold gas resides within a few disk scale lengths from the simulated galaxy centers. Figure courtesy of A. Brooks.

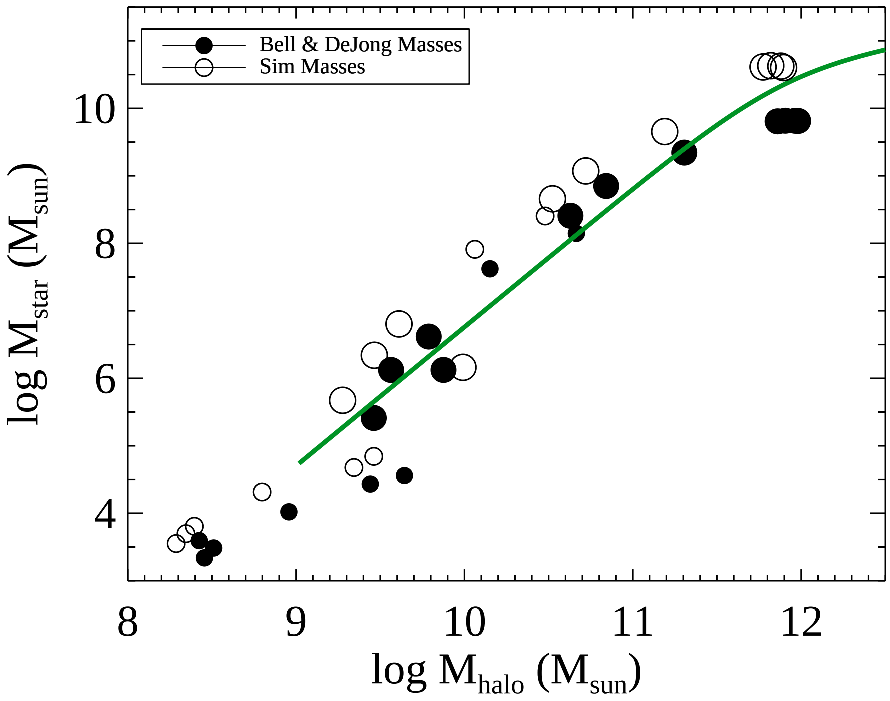

Figure 2.4 *The Stellar Mass vs Halo Mass.* Black Solid Dots: The SHM relation from our simulations set with stellar masses measured using Petrosian magnitudes and halo masses from DM-only runs. This procedure mimics the one followed in M12. Open Dots: Unbiased stellar masses measured directly from the simulations. Solid Line: Observational results from M12. Symbol sizes represent the different mass resolutions of galaxies in the sample. Smaller symbols are the better mass resolution by a factor of 8 when compared to the larger symbols.

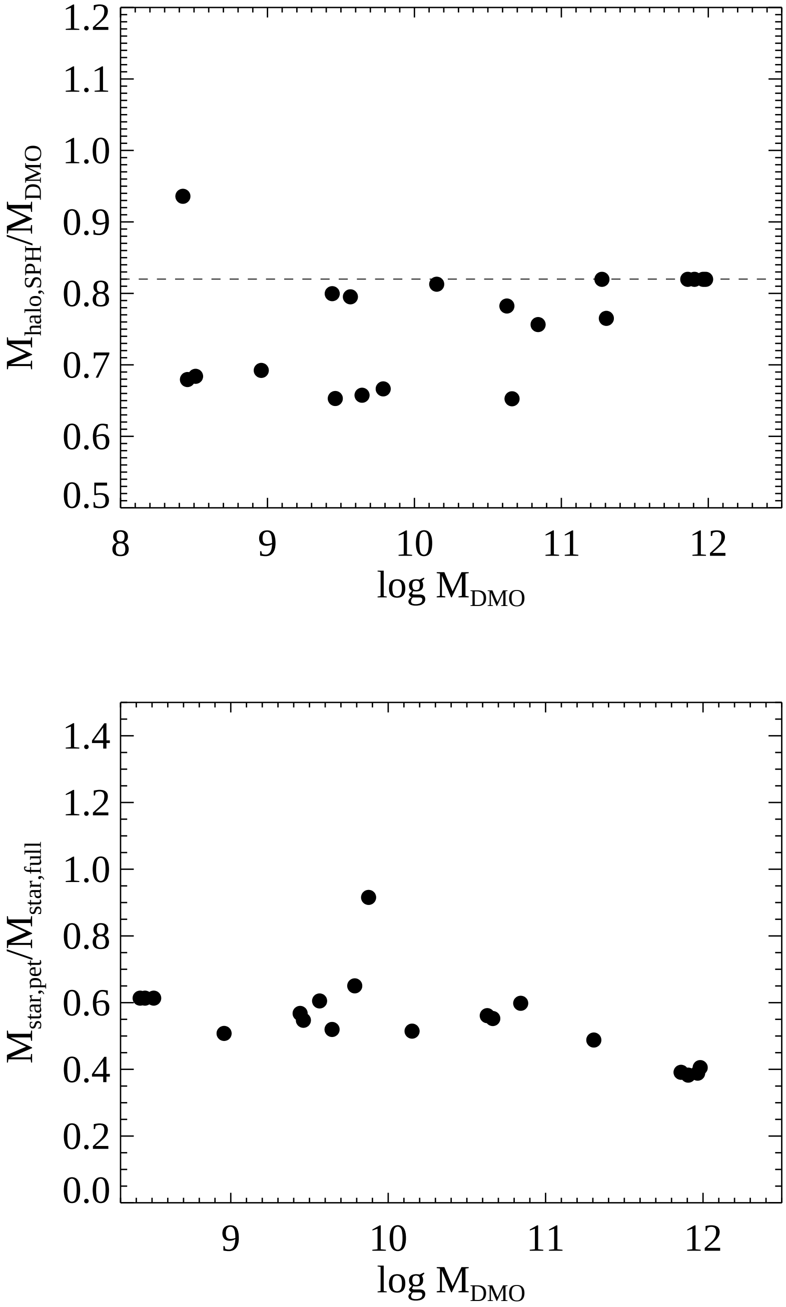

Figure 2.5 Top Panel: *Halo mass ratio of galaxies in runs with baryons and SF vs DM-only runs.* Individual halos in DM–only runs are typically 30% more massive than their counterparts in simulations with gas physics and SF. The effect is smaller in more massive halos, where baryon loss due to feedback is less (see also Sawala et al. (2012)). The dashed horizontal line marks the ratio if halos had a 100% baryon loss. Middle Panel: *Estimated vs. True Stellar Mass as a function of halo mass.* The stellar mass using artificial Petrosian magnitudes and measured using the photometric method in (Bell & de Jong, 2001) vs the "true" Stellar mass measured directly from the simulations. Stellar masses measured using the photometric method in (Bell & de Jong, 2001) in combination with the flux loss from applying the petrosian magnitudes are underestimated by about 50% across the range of galaxy masses in our study.

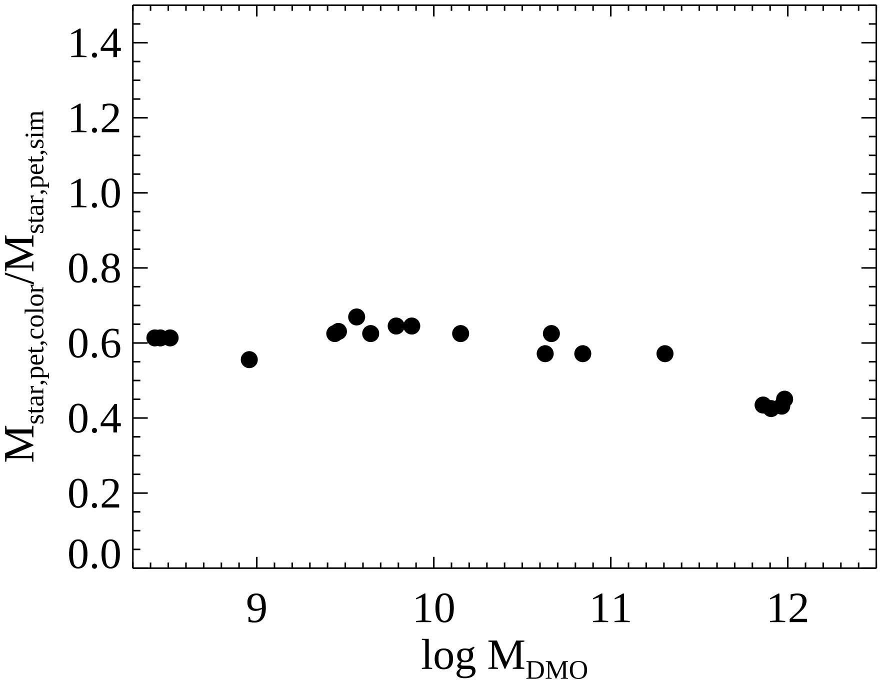

Figure 2.6 *Stellar mass within Petrosian radius using colors vs straight from simulations.* This highlights the contribution of using observational techniques in the underestimation of stellar mass, after the Petrosian radius is applied. The use of a fixed aperture underestimates mass by a further 10-20%, as previously estimated in Blanton et al. (2001)

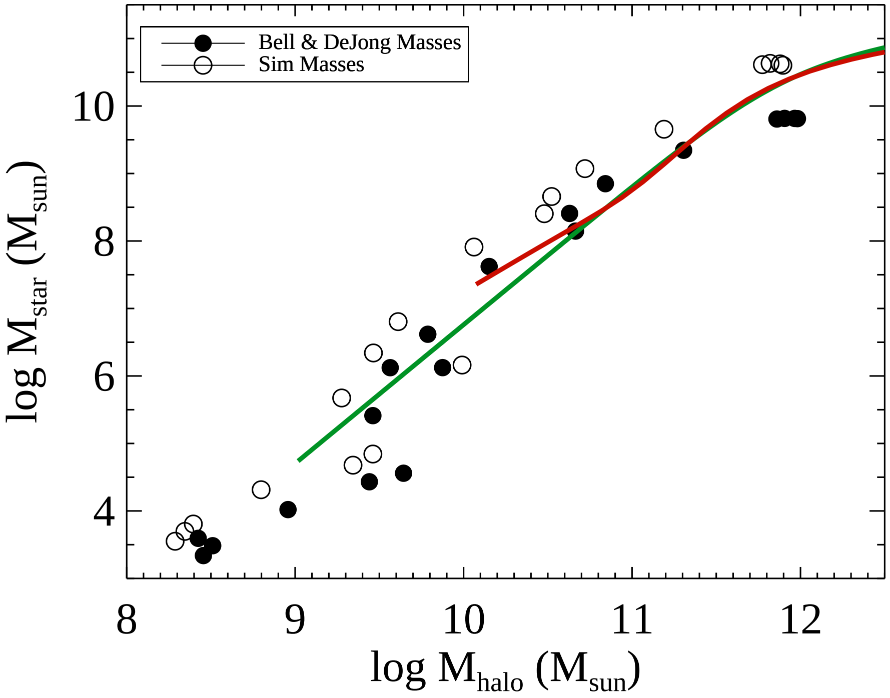

Figure 2.7 *The Stellar Mass vs Halo Mass.* Black Solid Dots: The SHM relation from our simulations set with stellar masses measured using Petrosian magnitudes and halo masses from DM-only runs. This procedure mimics the one followed in M12. Open Dots: Unbiased stellar masses measured directly from the simulations. Solid Green Line: Observational results from M12. Solid Red Line: Results from Behroozi 2012.

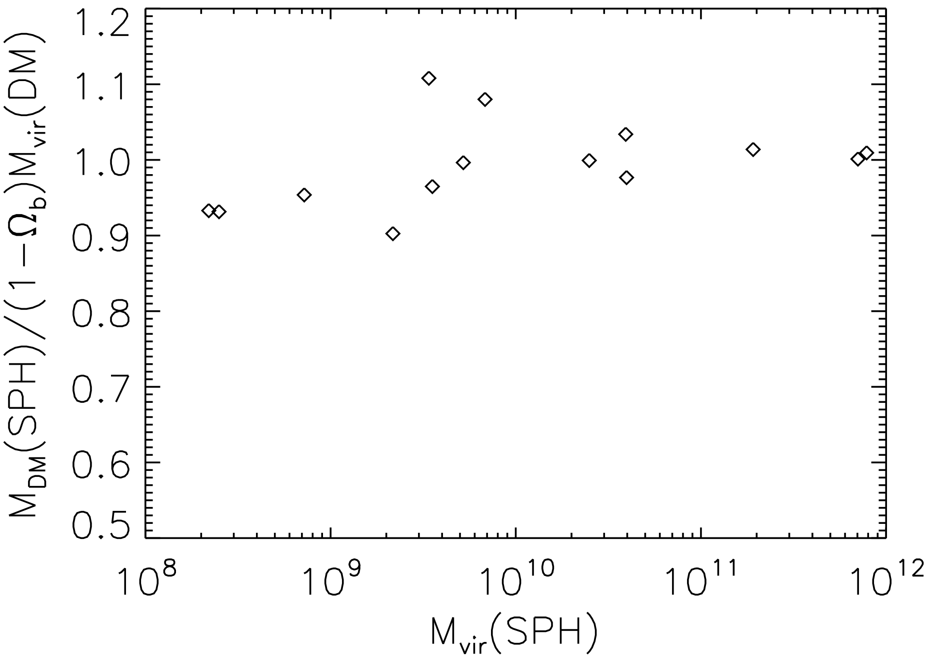

Figure 2.8 *Comparison of dark matter halo mass between a baryonic run and a collisionless run.* This figure shows that in the larger halos, the change in virial mass can be accounted for just by the change in overdensity after baryons are lost. However, in smaller halos, this is not sufficient: these halos must also suffer from reduced accretion, thus the scatter below 1. Figure courtesy of Alyson Brooks.

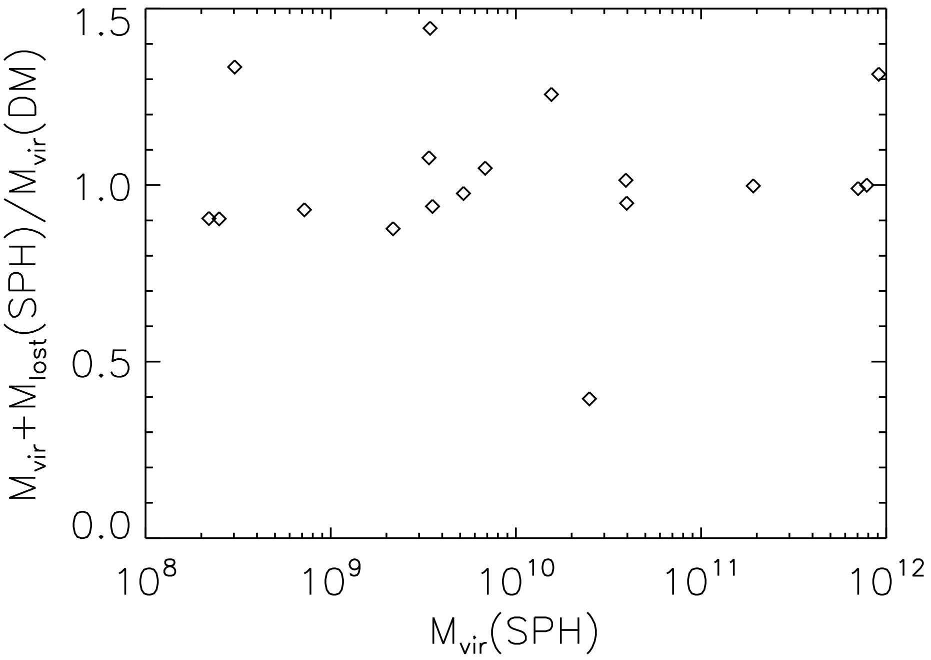

Figure 2.9 *Comparison of dark matter halo virial radius between a baryonic run and a collisionless run.* This figure, like the previous, shows that the change in virial radius is, in larger halos, due to the change in overdensity due to baryonic physics. In the smaller halos, this is not the case and these halos must have reduced accretion to account for the change in virial radius. Figure courtesy of Alyson Brooks.

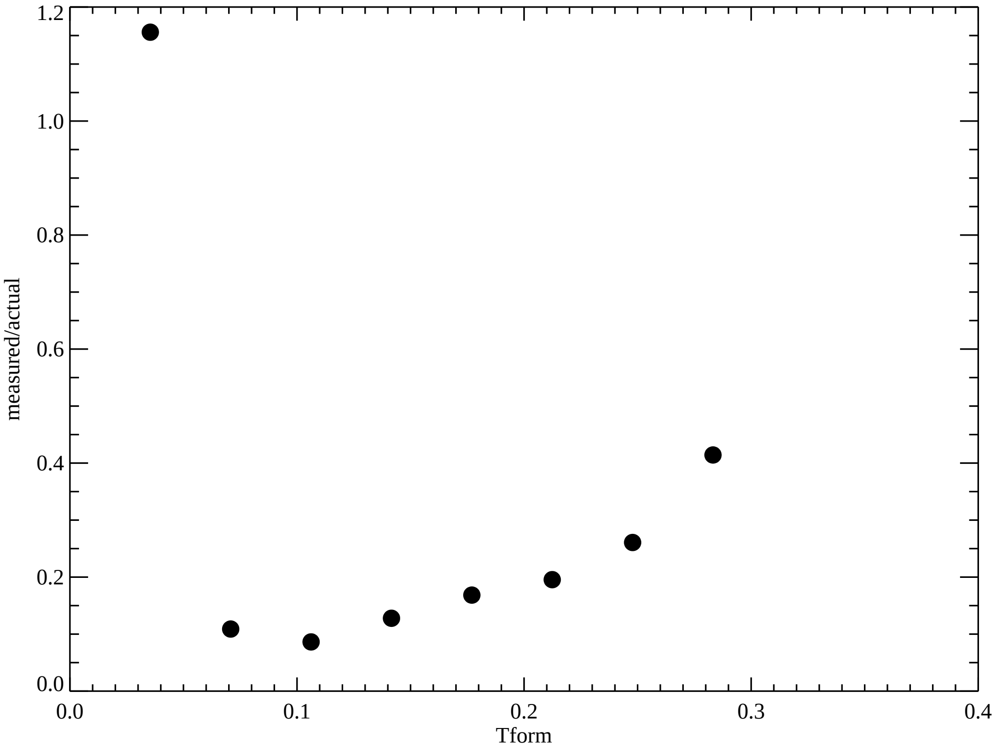

Figure 2.10 *Anyalysis of mass recovered as a function of stellar population age when using M/L ratios to estimate stellar mass.* In this figure, we use B-V color, as in the analysis for the SMHM relation. The first point is so high because the stellar population is so old that the B-V colors are undefined. The x-axis is time in simulation units, ranging from 0 to 13.7 Gyrs.

.

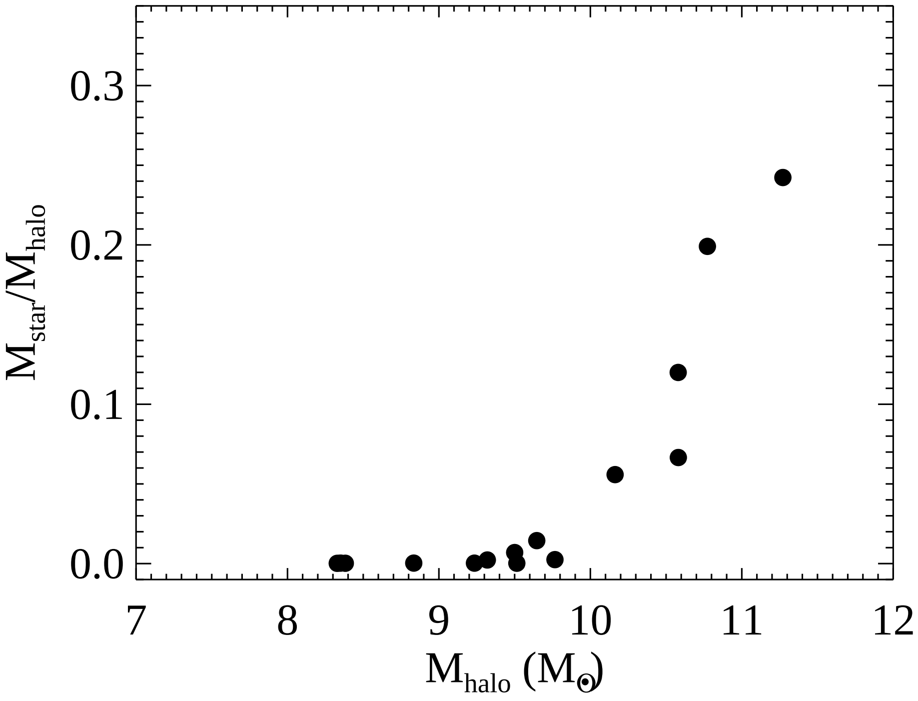

Figure 2.11 *Stellar mass in a given halo mass.* This figure shows how the star formation efficiency increases toward milky way halo masses.

.

Chapter 3

THE PRESSURE OF THE STAR FORMING ISM IN COSMOLOGICAL SIMULATIONS

Reproduced from Munshi et al. (2013a) with permission from the AAS.

We examine the pressure of the star-forming interstellar medium (ISM) of Milky-Way sized disk galaxies using fully cosmological SPH+N-body, high resolution simulations. These simulations include explicit treatment of metal-line cooling in addition to dust and self-shielding, H_2 based star formation. The 4 simulated halos have masses ranging from a few times 10^{10} to nearly 10^{12} solar masses. Using a kinematic decomposition of these galaxies into present-day bulge and disk components, we find that the typical pressure of the star-forming ISM in the present-day bulge is higher than that in the present-day disk by an order of magnitude. We also find that pressure of the star-forming ISM at high redshift is on average, higher than ISM pressures at low redshift. This explains the why the bulge forms at higher pressures: the disk assembles at lower redshift, when the ISM is lower pressure and the bulge forms at high redshift, when the ISM is at higher pressure. If ISM pressure and IMF variation are tied together as suggested in studies like Conroy & van Dokkum (2012), these results could indicate a time-dependent IMF in Milky-Way like systems, as well as a different IMF in the bulge and the disk.

3.1 Introduction

The origin of the stellar initial mass function (IMF) is paramount to our understanding of star formation, stellar evolution and feedback and galaxy formation. The IMF influences most of the observable properties of both stellar populations and galaxies. Detecting variations of the IMF will provide deep insights into the process by which stars form including but not limited to: the origin of the stellar mass scale, the effects of metallicity and environment and the energetics of feedback. Additionally, the IMF is a key ingredient into a huge range of models of all the above phenomena, and a necessary assumption when deriving physical parameters from observations. Despite being such a vital ingredient, the origin and variations of the IMF still remain poorly understood.

In particular, of critical importance, is the question of whether the IMF is universal or whether the IMF is sensitive to the initial conditions of star formation- i.e., the structure of the ISM in which the stars are forming (see e.g. Kroupa et al. 2011). Growing observational evidence suggests that the high mass behavior of the IMF is uniform, including observations of the IMF in the Magellanic Clouds (**?**Bastian et al., 2010; Chabrier, 2003). However at the low mass end, there are many indications, both observationally and theoretically, that there may be a variation in the IMF. For example, Conroy & van Dokkum (2012) and van Dokkum & Conroy (2011) show that the IMF in these systems is bottom heavy using gravity sensitive absorption lines in the cores of giant elliptical galaxies. This has also been independently suggested by kinematic and lensing data (Treu et al., 2010; Cappellari et al., 2012; Dutton et al., 2013). As these systems formed their stars at high redshift, these studies give us insight into the time-evolution of the IMF. Observationally, Conroy & van Dokkum (2012) show that the mass to light ratios of spheroidal systems indicate a more bottom heavy IMF at higher pressures, and at higher SFRs. This indicates that ISM pressure and the intensity of star formation are both key in understanding how and where stars form- and whether or not the IMF is varying.

Despite the importance of the IMF, a universally agreed upon, fully cosmological, physical theory of its origin and variation with environment has yet to be found: rather, many competing models exist. In particular, explaining the evolution of the IMF has been a challenge for theoretical models, especially in 'normal' systems. In general, these studies predict large IMF variations with local thermal Jeans Mass (Moore et al., 1999b; Larson, 2005), Mach number of the star-forming ISM, or the distribution of densities in a supersonically turbulent ISM (Padoan et al., 1997, 2012; Hennebelle & Chabrier, 2008; Hopkins, 2012b,a). Most theoretical models offer explanations of IMF variation in more extreme conditions-

ULIRG, nuclear starbursts owing to the extreme mergers and large gas inflows (Kormendy & Sanders, 1992; Hopkins et al., 2008; Hopkins, 2013; Narayanan & Davé, 2012; Narayanan & Hopkins, 2013) but many predict a top-heavy scenario, contradictory to the observational evidence. Furthermore, Krumholz (2011) shows that the critical mass, i.e. the fragmentation mass of a collapsing star-forming cloud, is dependent on the metallicity and pressure of the cloud itself. In a toy model, Weidner et al. (2013) suggest a time dependent IMF with a top heavy IMF slope followed by a prolonged bottom heavy slope which will bring the ISM pressure, temperature and turbulence into states that will drastically alter fragmentation of the gas, to explain observations.

In this letter, we perform SPH+N-body simulations of four medium-mass galaxies to directly explore the star-forming ISM in a cosmological context. This study is unique in that SPH simulations, being particle based, allow us to follow the full thermodynamic history of the gas. Furthermore, the resolution and star formation recipe in these simulations allow us to begin to probe the density structure of a more realistic star-forming ISM, in a cosmological setting. Here we specifically focus on a comparison between the star forming ISM of stars that make up the *present-day* bulge and those that make up the *present-day* disk. We find that stars form at ISM pressures an order of magnitude higher in the bulge than those in the disk, on average. Additionally, we find that at early times both bulge and disk stars form in a high pressure ISM. Finally, we find that differences in the formation radius of bulge and disk stars are not responsible for the different pressures. In short, we show that there ISM pressure varies with time, which could imply that the IMF varies with time as well.

3.2 The Simulations and Analysis

The simulations used in this work were run with the N-Body + SPH code GASOLINE (Wadsley et al., 2004; Stinson et al., 2006) in a fully cosmological ΛCDM context: $\Omega_0 = 0.26$, Λ=0.74, $h = 0.73$, σ_8=0.77, n=0.96. Using the 'zoomed-in' volume renormalization technique (Katz & White, 1993; Pontzen et al., 2008),we selected from uniform DM-only simulations field–like regions which we then resimulated at higher resolution. This set of simulations includes metal line cooling (Shen et al., 2010) and tracks non-equilibrium H_2 abundances (Christensen et al., 2012d, hereafter CH12). As in CH12, the star formation rate (SFR) in our simulations is set by the local gas density and the H_2 fraction; SF $\propto$ (f_{H_2} $\mathrm{c}_{*} \times \rho_{gas})^{1.5}$, with $c_* = 0.1$. Star formation is limited to gas with density greater than 0.1 amu/cc and temperature less than 3000 K, although the dependency of star formation on the H_2 abundance makes these limitations largely inconsequential. Tests of the convergence of star formation histories for this star formation perscription are described in CH12.

The full details of our SN feedback "blastwave" approach are described in several papers including, Stinson et al. (2006); Governato et al. (2012). As massive stars evolve into SN, mass, thermal energy and metals are deposited into nearby gas particles, with energy of 10^{51} ergs per event. Gas cooling is shut-off until the end of the snow-plow phase as described the Sedov-Taylor solution, typically ten million years. We also include gas heating from a uniform, time evolving UV cosmic background, which turns on at $z = 9$ and modifies the ionization and excitation state of the gas, following the model of Haardt & Madau (1996).The efficient deposition of SN energy into the ISM, and the modeling of recurring SN by the Sedov solution, should be interpreted as a proxy we have tuned to model the effect of processes related to young stars and to model the effect of energy deposited in the local ISM including UV radiation from massive stars (Hopkins et al., 2011b; Wise et al., 2012b). The simulations also include a scheme for turbulent mixing that redistributes heavy elements among gas particles (Shen et al., 2010). These feedback, star formation, and ISM parameters in simulations of the same resolution produced galaxies with realistically-concentrated bulges (Christensen et al., 2012b). Furthermore, it is important to note that because the simulations are tuned to produce realistic present-day galaxies (see e.g. Munshi et al. (2013b)), with correct surface densities, the mean ISM pressure in these simulations should be approximately correct, even if the feedback model does not include processes specifically related to young stars, stellar winds and radiation pressure (Hopkins et al., 2011b; Hopkins, 2013).

Galaxy Name	M$_{halo}$ (M$_\odot$)	Gas Particle Mass (M$_\odot$)	Softening (pc)
h986	1.9×10^{11}	3900	115
h277	6.8×10^{11}	3900	115
h258	7.7×10^{11}	3900	115
h239	9.1×10^{11}	3900	115

Table 3.1 Description of simulations utilized in this analysis.

We have simulated four different disk galaxies, at high resolution, described in Table 1. We dynamically decompose our disk galaxies based on cuts in angular momentum and energy(Scannapieco et al., 2011; Governato et al., 2009). Each star particle at $z = 0$ is traced back to the gas particle from which it formed in order in order to sample the properties of the ISM from which each component formed. Using the cold gas in the central few kiloparsecs of he galaxy, a star particle is established as disk when its specific angular momentum (j_z) is a large fraction of the angular momentum of a circular orbit with the same binding energy, i.e., $j_z/j_c > 0.8$. Using the potential of the entire matter distribution (dark, gas and stars), we determine the total energy for each particle and subsequently it's angular momentum. For the bulge and halo stars, star particles are identified based on their radial orbits and their binding energy: bulge stars have higher binding energies than halo stars. Furthermore bulge and halo are also distinguished by the radius where the spheroid mass profile changes to a shallower slope. We checked the stability of our kinematic decomposition across three simulation outputs in time- ie over the course of 100 Myr which approximates the dynamical time of the systems. We compared the results of our analysis in the case of the strictest definition that particles must be classified as the same component over a whole dynamical time to the weakest definition that particles need only be classified a component at $z = 0$ and found that the resulting trends remain unchanged.

Using full information from the simulations (kinematics, ages, metallicity), we have traced the density, temperature, velocity dispersion and pressure of the ISM in which the stars of each component form. Being particle based, the SPH approach of our simulations allows us to follow in detail the thermodynamical history of the gas through cosmic times, without resorting to additional 'tracer elements' (Genel et al., 2013). This allows us to examine not only where, but also *in what environment* stars are forming in our simulated Milky-Way like galaxies. In our analysis, we define pressure in very simple terms: $P = nk_bT$. We get temperature and density by tracing each star particle belonging to disk and bulge back to the gas particle from which it formed. Each gas particle is tagged with a local density and temperature that is a function of the simulation force resolution and softening length. Gas properties are calculated based on the 32 nearest neighbors. Our definition of pressure is limited to a “thermal” pressure term, which, as we do not resolve disks of highly turbulent gas, is actually a proxy for the entire pressure in the gas. Namely, it is the primary pressure support against the gravitational pressure in the disk.

3.3 Results

In this section we show that ISM structure is closely tied to star formation. Additionally, we show that at earlier times in a galaxy's history, stars are forming in a higher pressure ISM environment than that in which stars form today. This is theoretical evidence for a variation in IMF in a “normal” Milky-Way environment, if IMF variations are indeed tied to ISM structural parameters, like temperature, density, metallicity and pressure (Conroy & van Dokkum, 2012; Krumholz, 2011). For brevity, we show plots for one of our simulated halos, demonstrating the trends observed for all four halos.

In all four simulated halos, each cosmological and with varying merger and star formation histories, the distribution of pressure values in the ISM that forms *the present day* bulge is higher by an order of magnitude than that which forms the *present day* disk. In Figure 3.1a, we show the distribution of formation pressures for one of our simulated Milky-Ways, h986. The peak pressure of both distributions is different: bulge stars peak at pressures an order of magnitude higher pressure than disk stars. This shows that in general, bulge stars are forming ISM that is structurally different in terms of gas temperature and density: specifically, stars are forming from denser gas. It is important to note that the actual values for pressure are not comparable to pressures found in observations. As our star formation prescription is resolution limited, the maximum gas densities achieved are resolution dependent. What should be highlighted is the *relative* difference between the pressures found in the bulge and disk of our simulated galaxies. In Figure 3.1b and 3.1c, we show the SFHs for the 3 simulated halos, not directly discussed here, to show that in general, for all halos, the bulge forms at early times, and the disk forms later.

In Figure 3.2 we compare the phase diagrams for bulge and disk during a star formation event which contributes to the components' overall mass growth: for the bulge, this was between 2.5 and 4 Gyrs and for the disk, between 10 and 13 Gyrs. This figure at first glance, demonstrates that in general, the the bulge forms in a range of densities that is higher than that of the disk, and that the temperature range is very similar. Each point in the phase diagrams is color coded according to pressure where hotter colors represent higher pressures (red is the highest pressure bin). This color-coding further drives home that it is the high densities in the bulge star formation event that drive the high pressures, while in the disk, the high pressures result from higher temperatures. Since our simulations use an H_2-dependent star formation recipe, low metallicity gas particles would be expected to form stars at higher densities. However, from the bottom panel of Figure 3.2 is is clear that even at the same metallicities, bulge stars form from denser gas.

In Figure 3.3, we present the star formation history for the same galaxy, h986, for the dynamical bulge (red) and disk (blue). We also present the median pressure as a function of time for both components in the same time bins. Figure 3.3 highlights that both components are forming stars at higher pressures early in the galaxy's history. The star formation histories show that the bulge forms the majority of its stars early on, when typical ISM pressures are high, while the disk forms its stars later, when ISM pressures are lower. We also can see the parallel in the bulge SFH and the bulge pressure, in that bursts of bulge star formation seem to be contemporaneous with ISM pressure peaks. We discuss what this may imply in the summary.

Finally, in Figure 3.4, we explore whether formation location has any bearing on the pressure of the gas. We expect that pressure is higher closer to the center of the galaxy (i.e., where one would expect to find bulge stars), given that the vertical gravity and surface density should be higher closer to the center. As a result, one would expect high pressures towards the center of the galaxy. However, Figure 3 shows that this explanation cannot entirely explain the pressure differential between bulge and disk. In the top panel we see that there is no correlation between formation radius and pressure for either component, over the galaxy's whole history and that bulge stars are in forming at higher pressures than disk stars. In the second panel, we look only at the stars that formed in the early protogalaxy: specifically, the gas that forms stars that are 6 Gyrs old or more, when both components are should be at higher pressures. We see that with that cut, at any formation radius, bulge stars and disk stars are forming at high pressures in the early universe, implying the existence of an early high pressure star-forming environment in the protogalaxy.

3.4 Summary

In this letter, we provide evidence that ISM pressure is redshift dependent by examining the ISM pressures during the formation of the present-day bulge and disk. Because the present-day bulge predominantly forms early in the galaxy's history, it forms at higher pressures than the present-day disk. We show that in general, at early times, star formation occurs at higher pressures- specifically higher densities. We show that this is not the result of formation location and the higher densities found in the center of the protogalaxy: in general bulge and disk stars are forming over all formation radii. If ISM pressure and IMF are related as postulated in Krumholz (2011); Conroy & van Dokkum (2012), we have evidence for a redshift dependence of the IMF and further, that bulge stars formed with a different IMF from disk stars. Furthermore, we show that even at high redshift, bulge stars and disk stars in general, are forming at higher pressures, regardless of formation radius. This further supports the redshift dependence of ISM pressure: we see that in the young protogalaxy stars form in a high pressure disk, regardless of classification at $z = 0$. However, as Figure 3.3 demonstrates, the majority of bulge stars are formed in this high-pressure star formation epoch, while the majority of disk stars form in the later, low-pressure epoch. In our analysis we also examine the differences in metallically and H_2 fraction between bulge and disk, to isolate why the early protogalaxy is at high density (and thus high pressure). We find that bulge stars form from gas with higher H_2 fractions and even when holding metallicity constant, bulge stars form from denser gas. These trends point toward the high redshift progenitors having more dense gas, likely as a result of early rapid accretion.

Future work will include following the assembly history of these galaxies to determine the role of mergers and gas accretion in the formation of the present-day bulge and disk. We will follow the build-up of each component tracing each star back in time, including a full merger-tree. In this way we can determine isolate the role of mergers and in-situ star formation on the structure of the star-forming ISM

3.5 Supplementary Analysis

In this section I discuss supplementary figures that are not included in the analysis submitted to ApJL above. In the analysis below, I try to figure out why the pressure of the star forming ISM is time variant, resulting in the difference in pressure between bulges and disks in our simulations. In Figure 3.5, I examine the distribution of metallicities between bulge and disk to explore whether metallicity plays a role in the increased density that results in higher pressure at early times. However, metallicity peak for both the bulge and disk are very similar, although the disk component does have a high metallicity tail.

In Figure 3.5, I examine the distribution of H_2 mass fractions in the bulge and the disk and find that there is not a significant difference betwen the mass fractions in the bulge and disk of the galaxy, although the bulge, in general, has a slightly lower average H_2 mass fraction. I look at this more closely, by looking at the evolution as a function of time of the H_2 mass fraction over the course of a star formation event in each component (i.e. when that component was actively forming stars) in Figure 3.6. We see that on average, the disk has a lower average mass fraction over the course of it's burst when compared to that of the bulge.

Finally in Figure 3.7, I examine where on the phase diagram different values of H_2 mass fraction occur in the bulge: blue for high mass fractions, and red for low. In this plot it is interesting to note that all the high H_2 mass fractions correspond to the high densities in the phase diagram, meaning that there may be a correlation between an enhanced mass fraction and enhanced pressure.

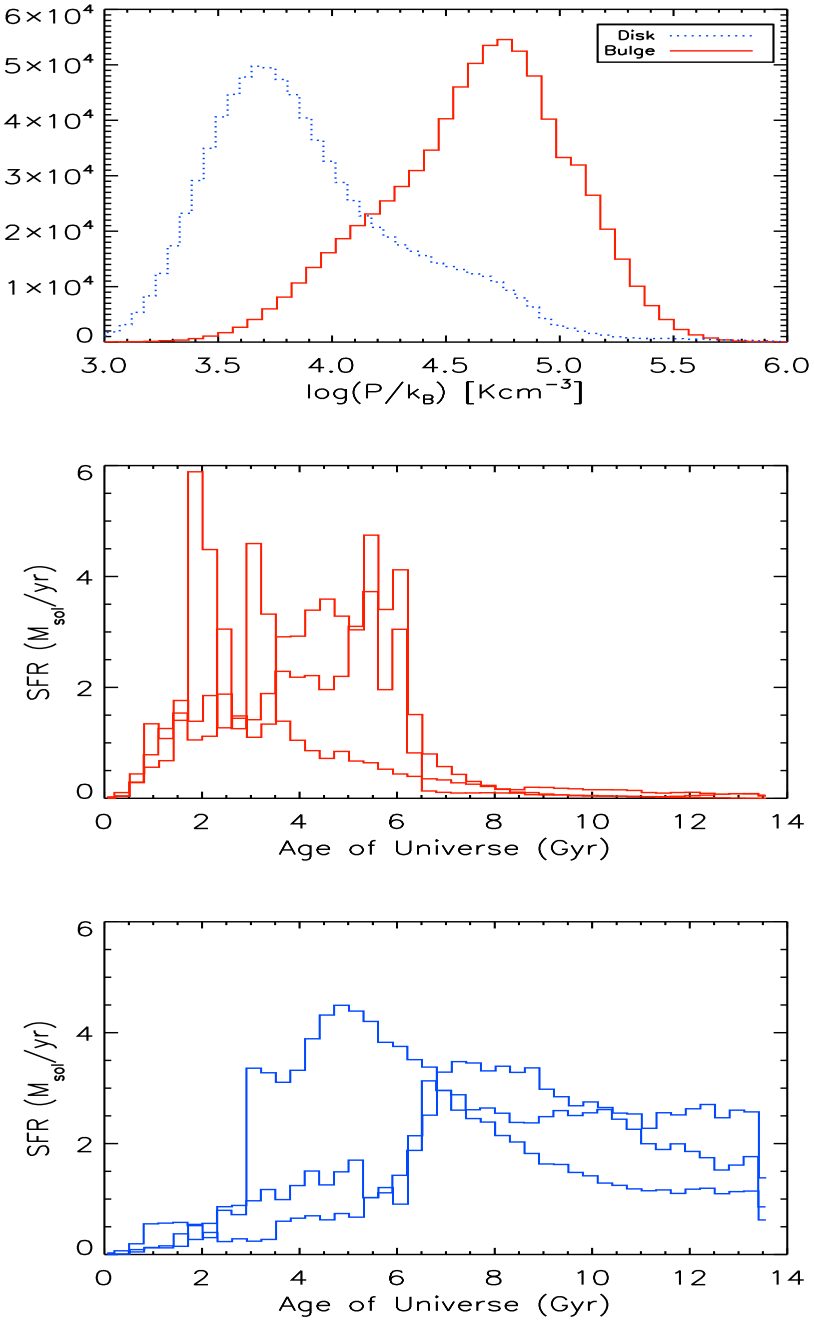

Figure 3.1 *Top Panel: Distribution of pressures for bulge and disk in one of the simulated galaxies, h986.* Note that the peak of the distribution of pressures of the bulge is higher than the peak of the pressure distribution of disk stars. *Middle Panel: SFHs for the bulges of the 3 galaxies not shown in this manuscript.* Note that like h986 shown in Figure 3, the bulges form early in the galaxy's history. *Bottom Panel: SFHs for the disks of the 3 galaxies not shown in this manuscript.* As with the bulges, these galaxies also follow the same trend as h986, with disk star formation occuring later in the galaxy's history.

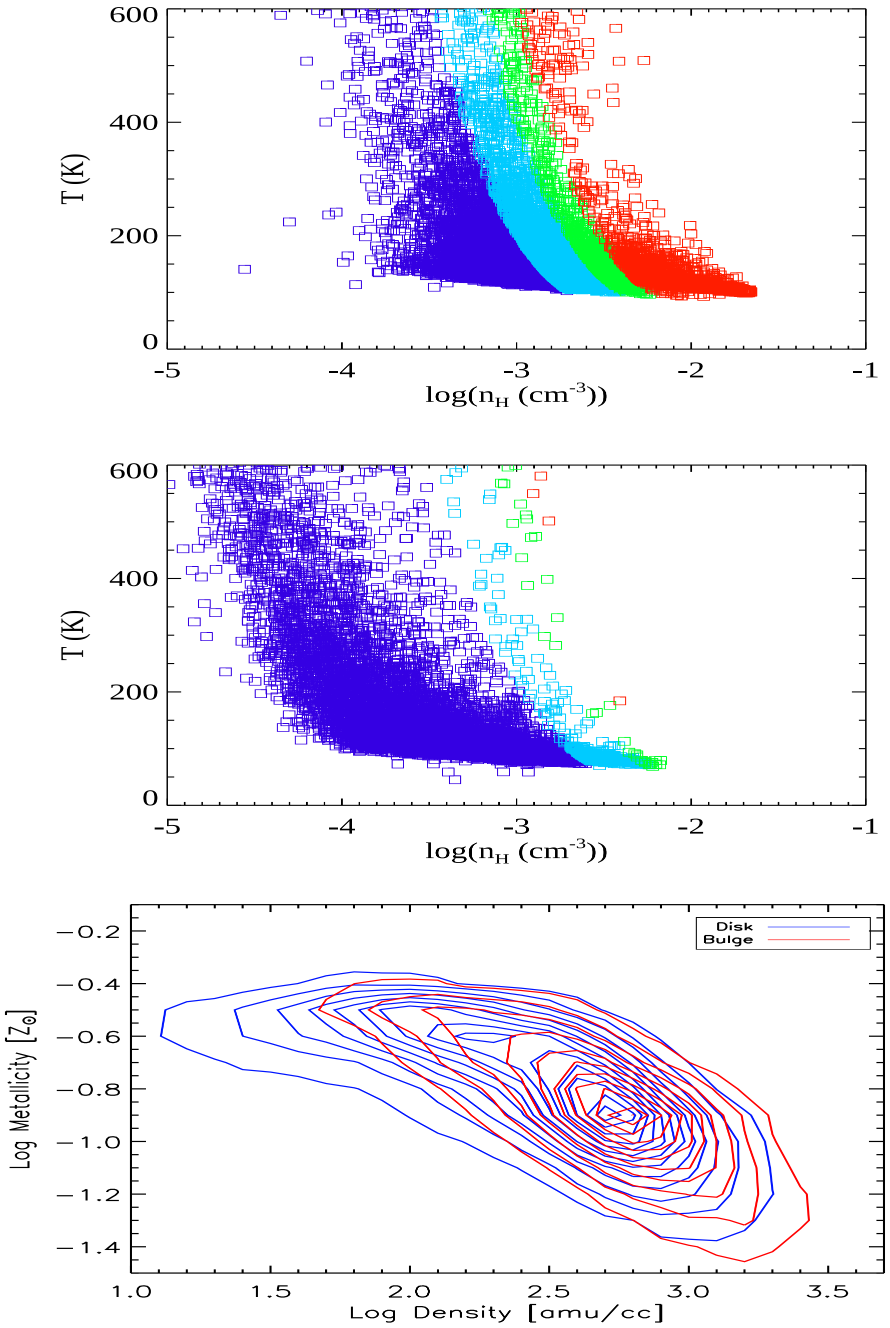

Figure 3.2 *Phase Diagrams for bulge (top) and disk (bottom) during a star formation event, color coded by pressure.* Star formation events for each component were selected based on contribution to each components' overall growth. Hotter colors are higher pressures, cooler colors are lower pressures. Note that high pressures are driven by high densities in the bulge. In the bottom panel we show the metallicity of the gas that formed both the bulge and disk stars versus its density at the time of star formation (note that both density and metallicity are smoothed over hundreds of parsecs).

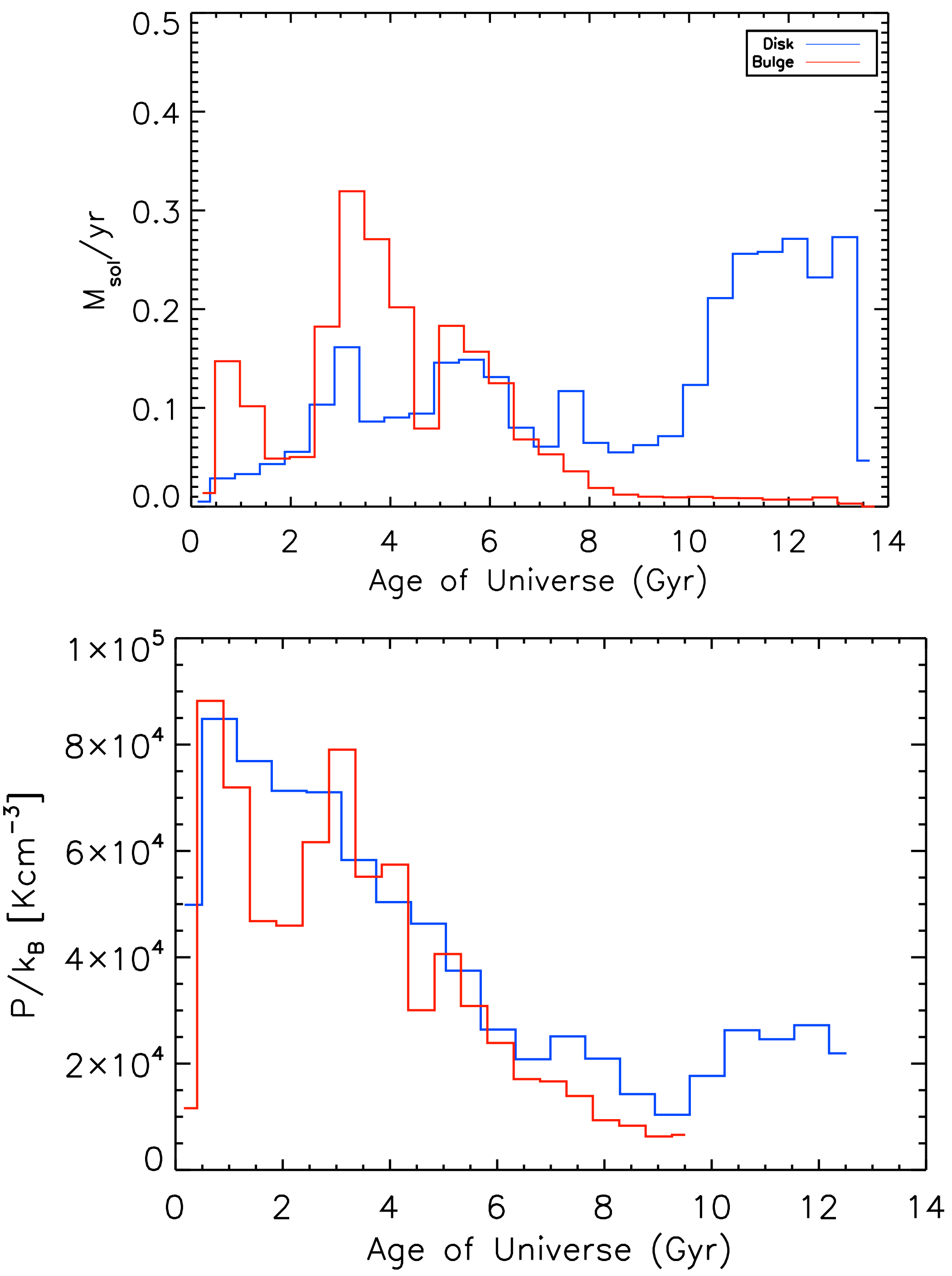

Figure 3.3 Top Panel: *Star formation rates for each of the dynamical components of h986.* Bottom Panel:*Pressure vs. Time for each of the components.* This highlights the redshift dependence of the pressure of the star forming ISM: early on, stars are forming at higher pressures, regardless of which component they belong to at $z = 0$. Note also the peaks in pressure are present when the SFH is peaking, in bulge stars. The big bursts in the bulge SFH correspond to major mergers in the galaxy's history.

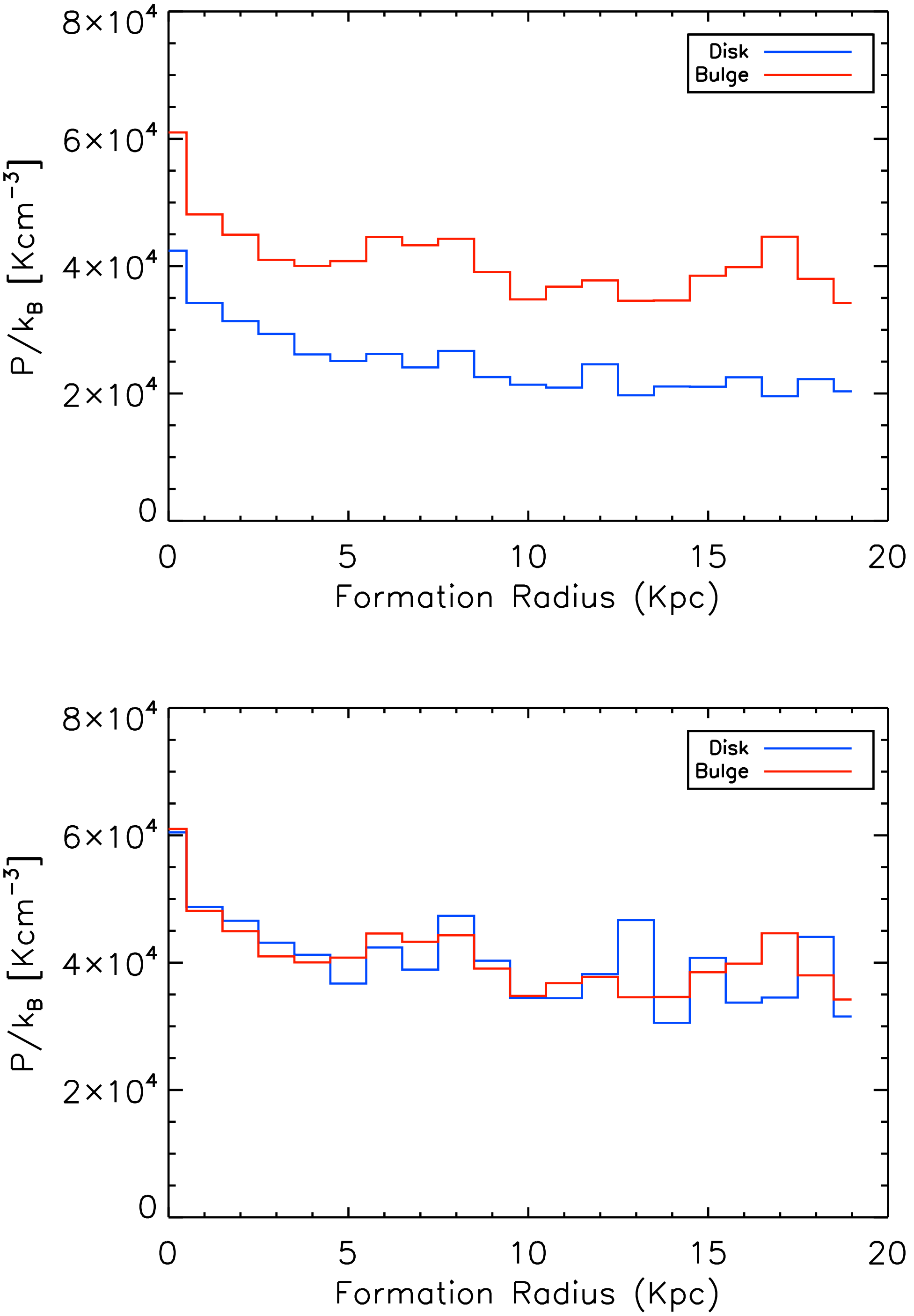

Figure 3.4 Top Panel: *Pressure vs. formation radius for the bulge and disk, over the galaxy's whole history.* Bottom Panel:*Pressure vs.formation radius for each of the components, for stars that formed before 6 Gyrs (when the pressure of the ISM was higher for both components.* This figure highlights that formation radius is not the underlying cause of the pressure differential between bulge and disk and that on average, bulge stars are forming at higher pressures than disk stars. The bottom panel shows that in the first half of the galaxy's history, stars are forming at higher pressures in general, regardless of component and formation radius.

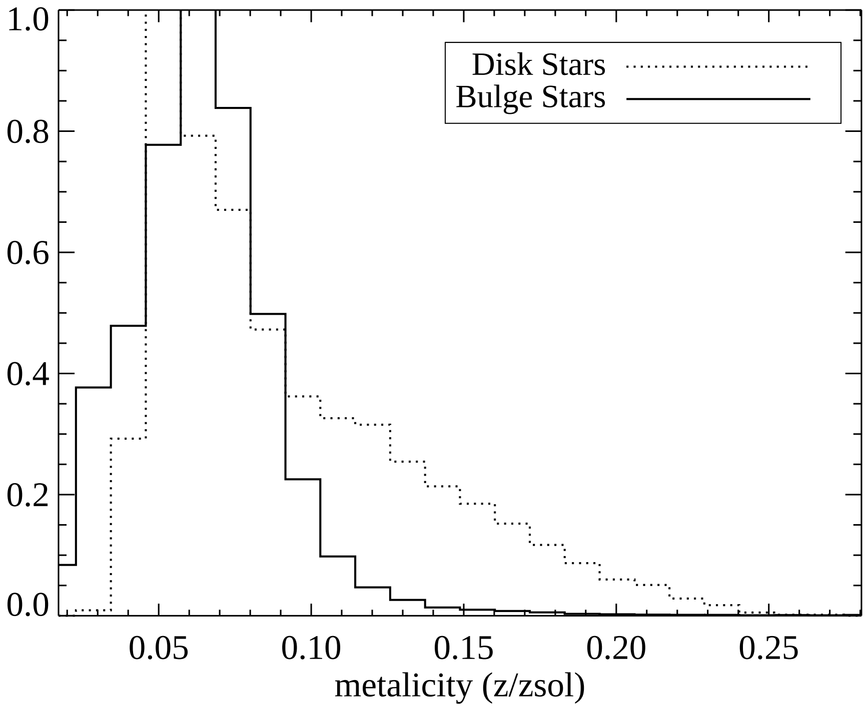

Figure 3.5 *Distribution of metallicities for bulge and disk in one of the simulated galaxies.* Note that the peak of the distribution of pressures of the bulge and disk are nearly the same.

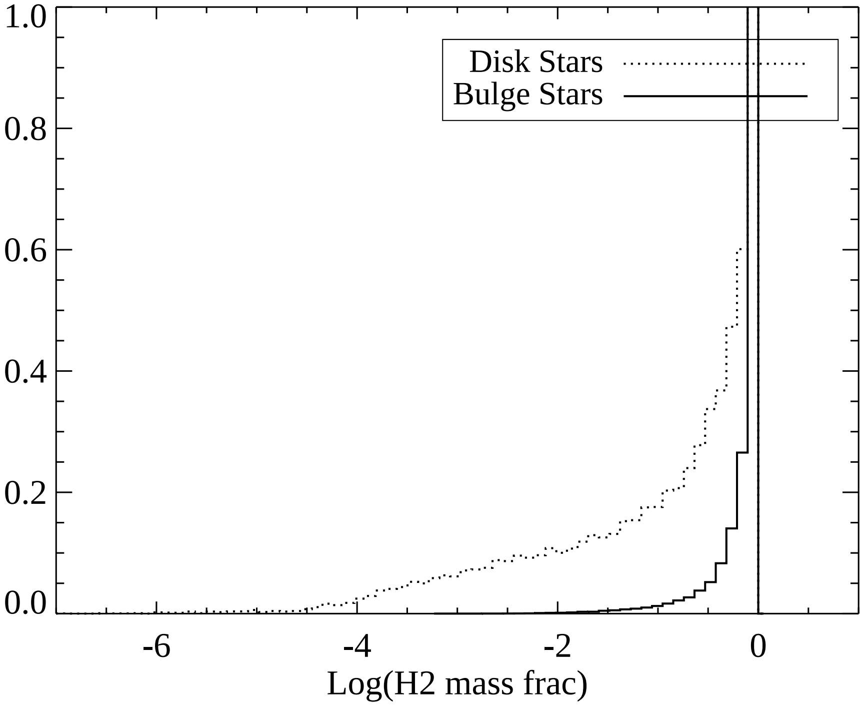

Figure 3.6 *Distribution of* H_2 *mass fractions for bulge and disk in one of the simulated galaxies.* Note that the peak of the distribution of pressures of the bulge and disk are nearly the same.

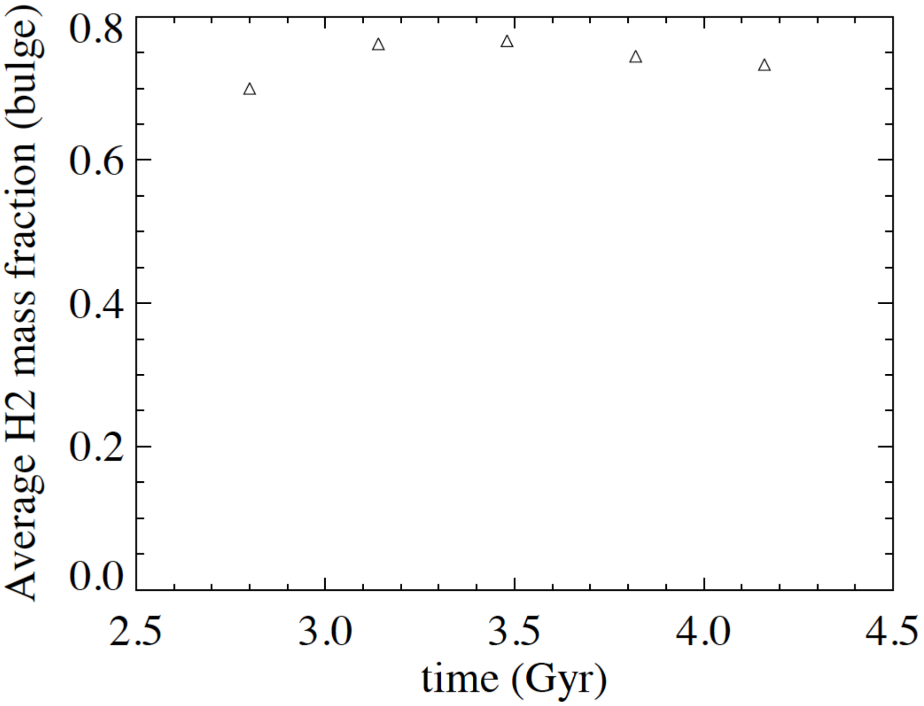

Figure 3.7 *Average H_2 mass fractions for the bulge as a function of time, during a star formation event.*

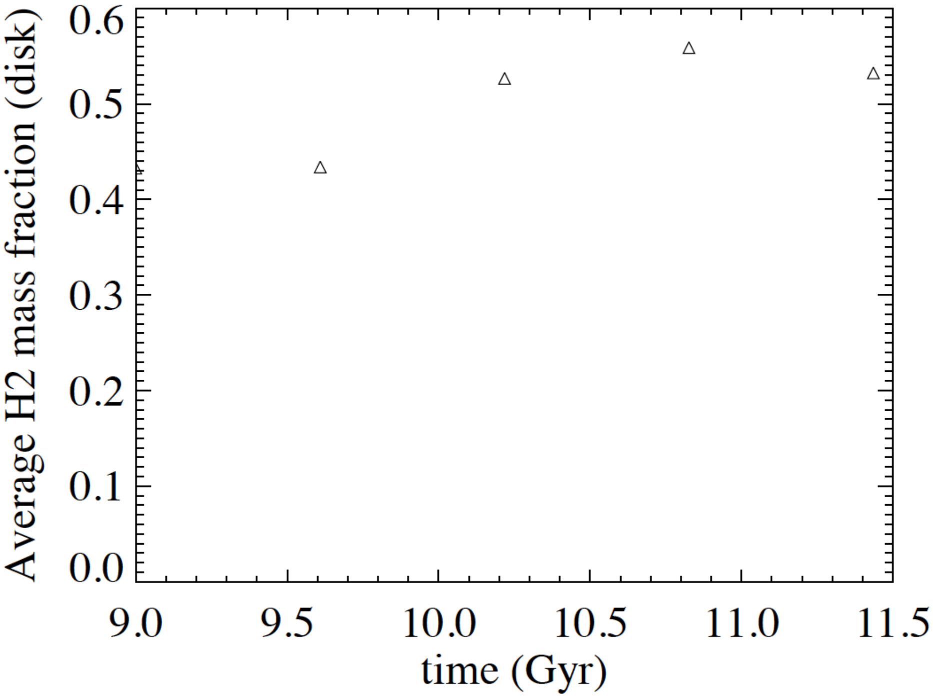

Figure 3.8 *Average H_2 mass fractions for the disk as a function of time, during a star formation event.*

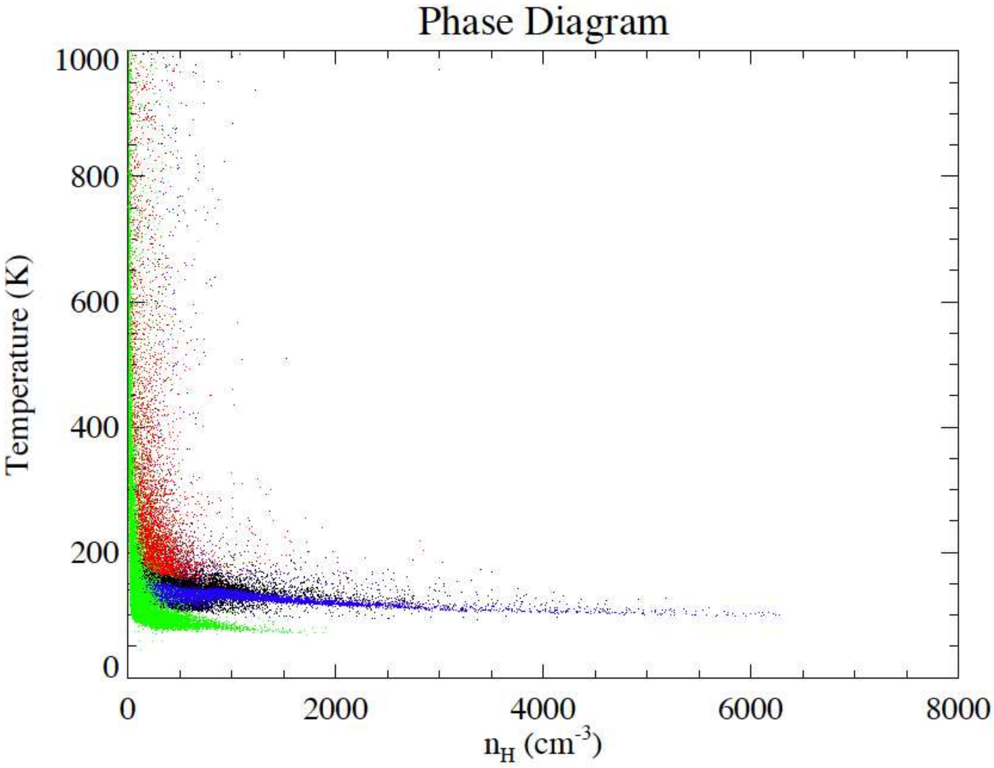

Figure 3.9 *Phase diagram for bulge stars color coded by H_2 fraction.* Blue points are high H_2 fractions, and red points are low H_2 fractions.

Chapter 4

DWARFS AND STAR FORMATION (SF) INDICATORS: ARE SF INDICATORS SENSITIVE TO TIMESCALE?

In this chapter, I discuss early work-in-progress results on dwarfs and star formation indicators. I use observational techniques to measure star formation rates in dwarf galaxies, using simulated observations generated from the postprocessing software, SUNRISE. We show that our cosmological dwarf galaxy simulations have star formation rates similar to those observed locally, in the LVL sample (observational data courtesy of Weisz et al. (2012)), regardless of star formation recipe and resolution. Further, we show preliminary analysis of the timescale dependence of SFR on the indicator used.

4.1 Introduction

Observations of star formation rates (SFRs) of galaxies provide vital clues into the history of the galaxy and are key probes into the evolutionary history of the galaxy. Different types of galaxies along the hubble sequence contain a wide range of young stellar content and star formation activity. Understanding this variety and its origin is fundamental to understanding galaxy evolution in the context of it's stellar populations.

Hα nebular line emission and the UV continuum are two widely used star formation rate (SFR) indicators. The Hα emission traces the recombination of the gas ionized by the most massive stellar population, and therefore traces star formation over the lifetime of these massive O and B stars (masses greater than 20 solar masses). UV flux, on the other hand, originates from the photospheres of stars from O through later B type stars (any stars greater than 3 solar masses) and thus measures a longer timescale: averaged over nearly 10^8 years. Both tracers should yield consistent SFRs as both are tracing the young stellar population in galaxies. Discrepencies between the two measures reveal problems either in the calibration of these indicators, or more fundamentally, the assumptions in converting these fluxes into star formation rates. Star formation rates from indicators are generally derived assuming this functional form: SFR = K(λ)×F(λ), where K(λ) can be inferred from population synthesis models under several assumptions, including a functional form of the IMF. This assumes a universal IMF, regardless of morphological type, luminosity and redshift. Additionally, it assumes certain timescales of star formation: for example it has been shown that a bursty star formation history, like that expected in dwarfs, can cause variations in the indicators, such that they do not trace each other (Mateo, 1998).

Many studies have directly compared the integrated Hα and UV SFRs for which both diagnostics have been measured (Buat et al., 1987; Buat, 1992; Bell & Kennicutt, 2001; Salim et al., 2007). Normal spiral galaxies show broad agreement between the two indicators, with the correct treatment of dust attentuation and extinction (they find that UV is the most impacted by extinction). As lower mass regimes are probed, as mentioned above, there are indications that the flux ratio systematically decreases and that Hα flux is systematically lower when compared to the UV (Bell & Kennicutt, 2001). This trend could mean many things: recent star formation histories of these galaxies are bursty or abrupt and it could also mean, the IMF is not universal and becomes more deficient in the highest mass stars in these low mass, low surface brightness systems.

In this chapter, I will address how I used simulated dwarf galaxies in an attempt to track what is going on with these star formation indicators. I first discuss the simulations that I used in this analysis and the affects of resolution. Then I discuss the software I used to create the artificial observations used for making measurements. I show the agreement between the simulations and the observed trends with mass.

4.2 The Simulations and Analysis

The production-run simulations used in this chapter were, as were all the other simulations, run with the N-Body + SPH code GASOLINE (Wadsley et al., 2004; Stinson et al., 2006) in a fully cosmological ΛCDM context: $\Omega_0 = 0.26$, Λ=0.74, $h = 0.73$, σ_8=0.77, n=0.96.

This set of simulations includes metal line cooling (Shen et al., 2010) and non-equilibrium model for H_2 abundance, which includes formation on dust grains, destruction by Lyman-Werner radiation and shielding of both HI and H_2 (Christensen et al., 2012d), as described in detail in chapter 2.

The older, lower resolution simulations used in this chapter were also run with GASOLINE with the same cosmology, and like the production-run simulations, selected from uniform DM-only simulations of 25 Mpc per side. The same field–like regions were selected and resimulated at higher resolution, but these were resimulated at *half* the effective resolution of the new simulations described above. These simulations incorporated detailed metal cooling and turbulent mixing in the ISM. There is a metallicity dependent radiative cooling included at all the temperatures in the range of 100-10^9 K. The cooling function is determined using pre-computed tabulated rates from the photoionization code CLOUDY (Ferland et al., 1998a), folowing Shen et al. (2010). These values assume that metals are in ionization equilibrium and the ionization, cooling and heating rates for primordial species are calculated time-dependently from the rate equations.

Both sets of simulations utilized the “blastwave” SN feedback approach. As in previous works using the “blastwave” SN feedback approach (Stinson et al., 2006; Governato et al., 2012), mass, thermal energy, and metals are deposited into nearby gas when massive stars evolve into SNe. The amount of energy deposited amongst those neighbors is 10^{51} ergs per SN event. Gas cooling is then turned off until the end of the snow plow phase of the SN blastwave. Equilibrium energy rates are computed from the photoionization code Cloudy (Ferland et al., 1998b), following Shen et al. (2010). A spatially uniform, time evolving, cosmic UV background turns on at $z = 9$ and modifies the ionization and excitation state of the gas, following an updated model of Haardt & Madau (1996). The simulations also include a scheme for turbulent mixing that redistributes heavy elements among gas particles (Shen et al., 2010).

Interfacing GASOLINE with SUNRISE (Jonsson et al., 2010; Jonsson, 2006) allows us to measure the SED of every resolution element of our simulated galaxies from the far UV to the far IR with a full 3D treatment of radiative transfer. SUNRISE includes a realistic description of the effects of dust reprocessing: an important source of bias in observations (Narayan 2010). The latest version enables us to make detailed calculations of images, spectra and integral field unit-type outputs of line-of-sight velocity distributions, accurately accounting for the scattering and differential attenuation of light from different populations along the line of sight. In this analysis, we utilize the extensive library of filters ranging from GALEX FUV through Spitzer MIPS, as well as create our own filter, for the Hα line to compare the broadband flux with the lineflux from the SUNRISE generated SED.

In Figure 4.1, we show the relevant portion of the SUNRISE SED, showing the Hα line from which we measure the lineflux to derive a SFR. In Figure 4.2, we show a mock-image generated by SUNRISE, in the FUV, of one of our dwarf galaxies. In Figure 4.3, we show the same mock image convolved with GALEX's PSF, which creates the final image from which we make our measurement. Our FUV measurements of flux follow the flux measurement techniques utilized by the observers when making their measurements (i.e., we perform our photometry using the methodology outlined on the GALEX website). We obtain Hα lineflux measurements by measuring the continuum of the artificial SED for the 100-300 angstroms adjacent to the line. We then measure the flux of the line for various widths, based on fitting a gaussian line profile to the line to get a baseline width. I also developed code to create artificial Hα images using SUNRISE by creating a narrow-line filter to add to the SUNRISE library.

4.3 Results

In this section we show the mock images generated by SUNRISE, as well as the relevant portions of the SED utilized in this analysis. We also show that measurements of star formation rate based on these mock images and SEDs result in good agreement between simulations and observations. In figure 4.4, we show the relationship between the star formation rate derived from UV to that derived utilizing the Hα lineflux from the SED using our current production-run simulations that include H_2 based star formation, and

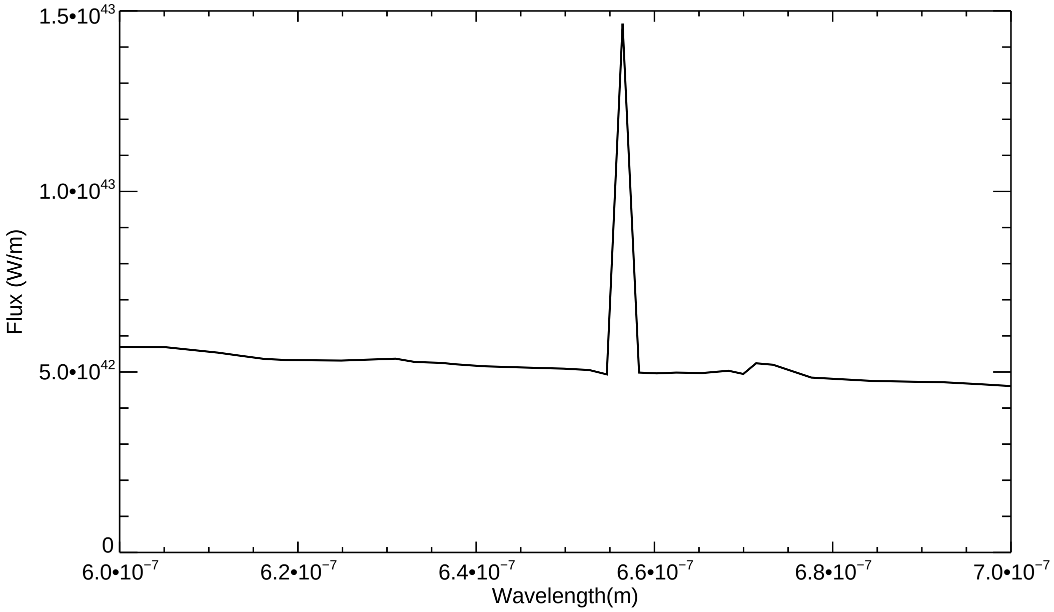

Figure 4.1 *Simulated observation of Hα emission from SUNRSISE SED.* The lineflux from this line is used to derive SFR in simulated dwarfs, normalized by continuum measurements in the simulated SED.

double the resolution. We show that the simulated galaxies follow the general trend of the observed galaxies (black points), in the mass range probed by our simulations. In Figure 4.5 we show the ratio of SFRs derived in the low resolution, metal-line cooling simulations. For some of the galaxies, we also show the z=0.5 ratio to see if there is a time dependence to the agreement between simulations and observations. Again, even with the different cooling model, and lower resolution, the simulations show broad agreement with the trends shown in the observational data.

In Figure 4.6 we show a comparison between a star formation history for the same dwarf in the low resolution metal-line cooling run, and the high resolution H_2 run. We note that the former forms more stars over the galaxy's history and has in general, what appears to be a more bursty star formation history (SFH). In the newer run, there is less star formation and the SFH is less punctuated with big bursts at early times. However, we note that in

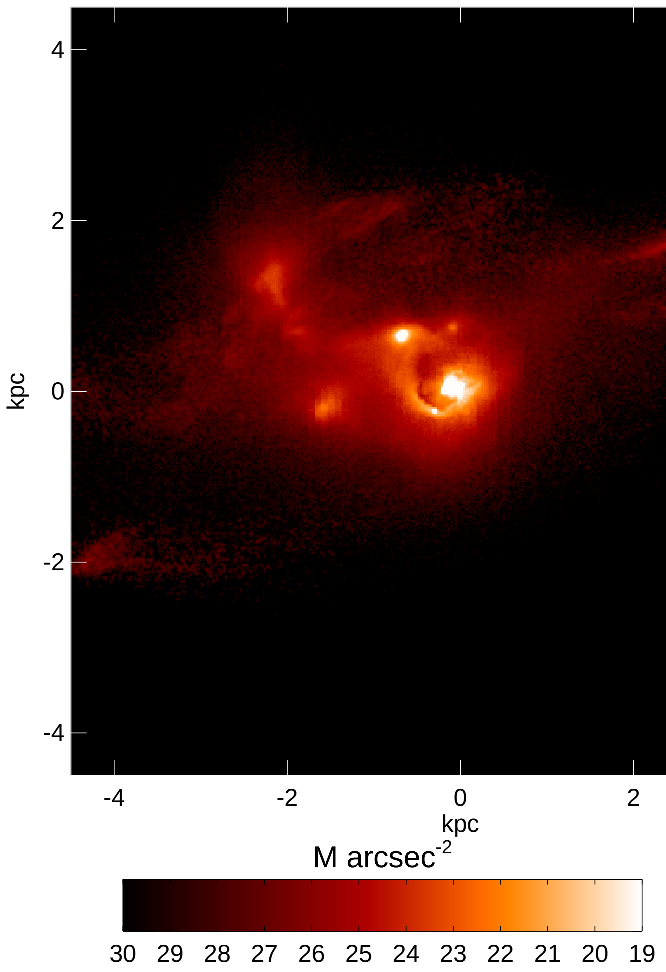

Figure 4.2 *Simulated observation of 24 micron emission from SUNRISE.* The flux from thses images is used to derive SFR in simulated dwarfs.

the last 4 Gyrs, both galaxies have a quiescent, relatively constant SFR. Both runs have SFRs derived from the indicators that are consistent ($0.03 M_{sun} yr^{-1}$). As the star formation indictors are tuned such that they are sensitive to recent star formation, we expect there to be agreement between the runs, as they differ mainly at early times in their star formation history. This regime is where the low resolution run produces more stars, which should not

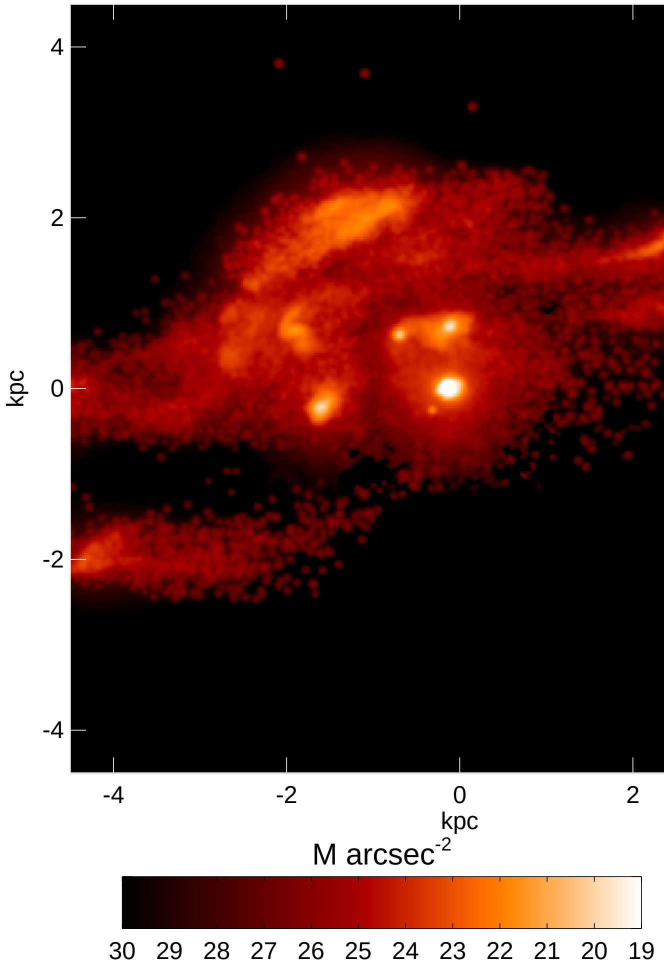

Figure 4.3 *Simulated observation of UV emission from SUNRSISE generated image, including dust reprocessing.* The flux from such images are utilized to derive SFRs.

change measurements derived from indicators probing young populations.

In Figures 4.7 and 4.8, we examine measured SFR from an indicator compared to the actual SFR from the simulation, integrated over various timescales. We expect that if a given indicator is most sensitive over a specific timescale, the recovery of the true SFR will be closer to 1. However both these plots for the UV and Hα are inconclusive. Niether

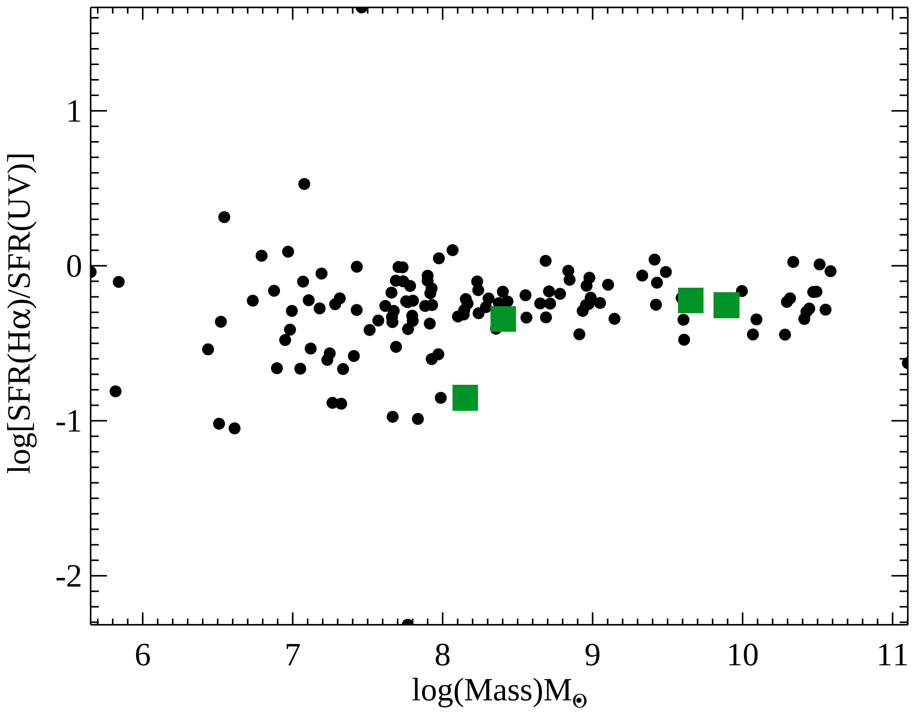

Figure 4.4 *Ratio of SFRs derived from the UV continuum and from Hα.* Stellar mass is on the x-axis, and the ratio of SFRs from the various indicators are on the y-axis. Green squares are the simulations, and the black points are the data from Weisz et al. (2012).

indicator seems to recover SFR well, no matter the timescale. Additionally, the time trends are not what is expected- we are seeing good recovery at 1 Gyr, although neither indicator should have better sensitivity on such a long timescale. We expect that this may be a mass effect: these halos are too massive to distinguish the mass effect as we'd expect stronger trends in lower mass halos. In smaller halos feedback shuts off the star formation entirely for some period of time. As a result, Hα shuts off very quickly, and the UV, sensitive to less massive stars, will linger a bit longer. However, in these more massive halos, there is always a low level of SF resulting in there always being both Hα emission and UV flux.

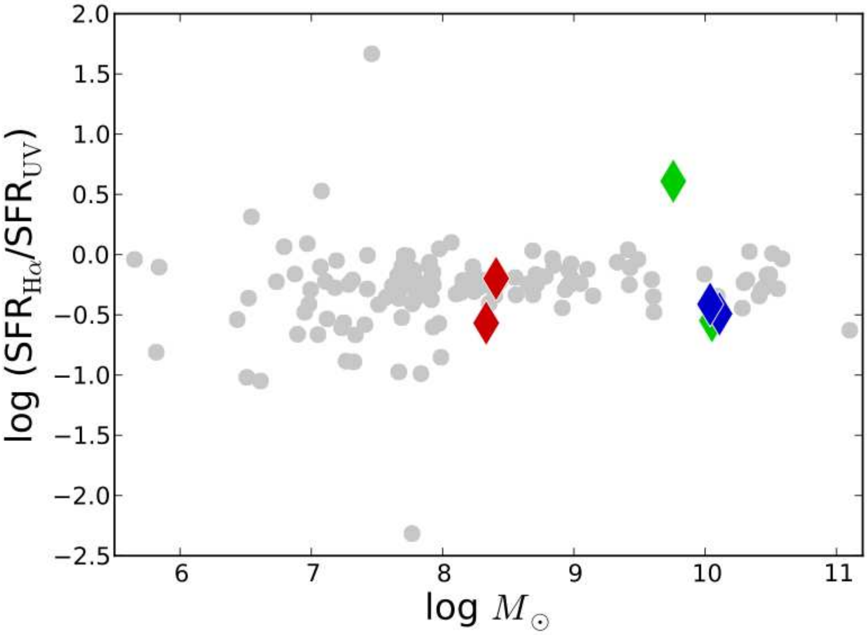

Figure 4.5 *Ratio of SFRs derived from the UV continuum and from Hα, utilizing lower resolution simulations, with only metal-line cooling.* Each color represents a different dwarf simulation; if more that one point exists for a given color, one point is z=0 and the other is at z=0.5. The greyed out points in the backgroud once again are the observational data from Weisz et al. (2012).

4.4 Summary

In this chapter, I show that there is broad agreement between SFRs derived from simulated dwarf galaxies, and those derived from observations. I show that even with changing the star formation model and the resolution of the simulations, we still show agreement between simulations and observations. Further study would include tracing the time-dependence of these indicators over the course of a star formation burst to see how sensitve the star formation indicators are to the burstiness, and when during a burst, you are probing the galaxy.

My work in progress includes running an extremely high resolution sheet of dwarf galaxies, using the newest version of GASOLINE, ChaNGa, which fixes the problems associated with traditional SPH simulations. Using this new sample of dwarfs, I will be able to probe a lower mass regime and study the time scale dependence of the indicators in greater detail over a lower mass range that has greater inconsistency between indicators in the observational data.

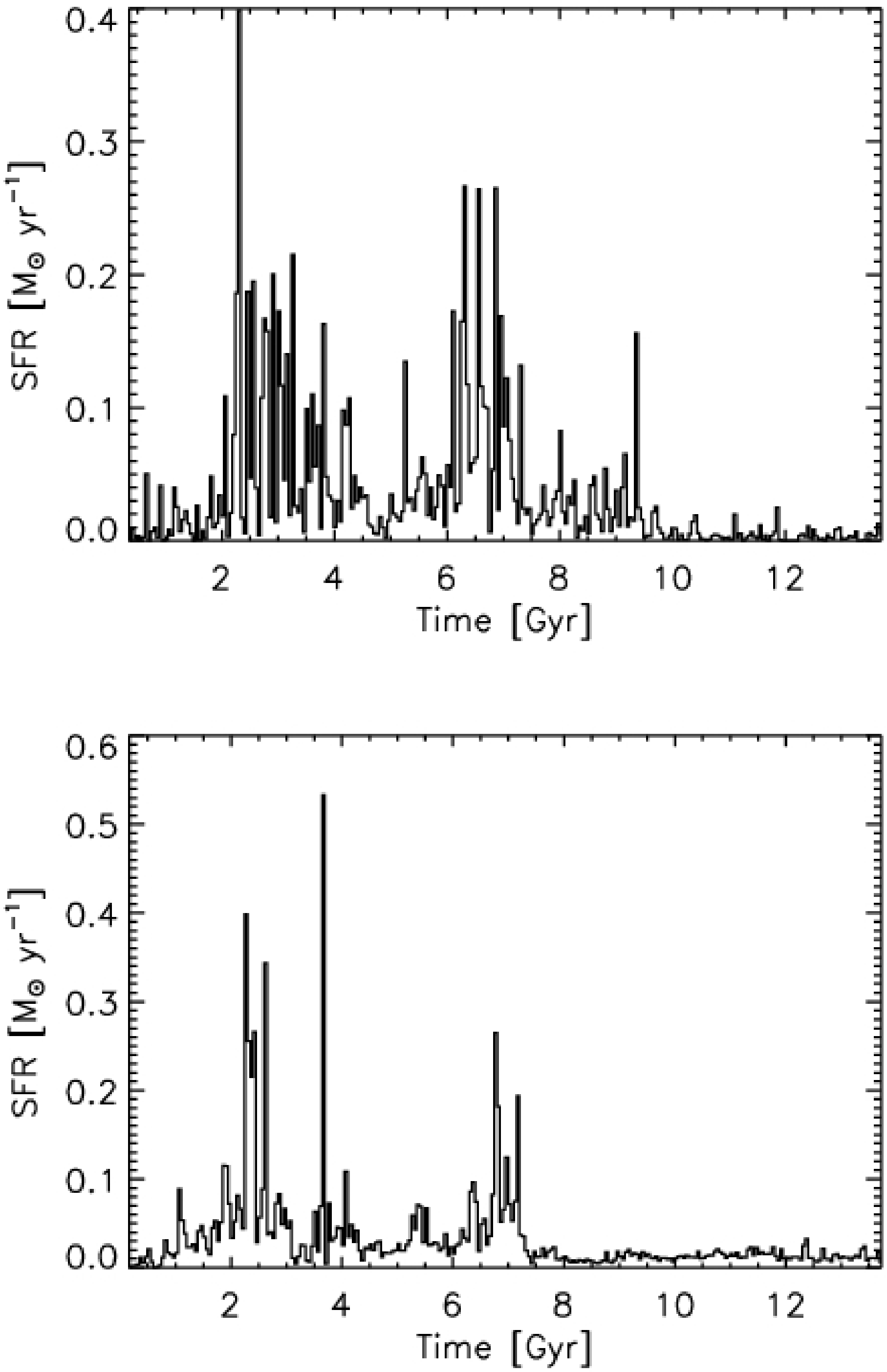

Figure 4.6 Top Panel: *Star formation rate for the lower resolution, metal-line cooling run.* Bottom Panel:*Star formation rate for the high resolution, H_2 star formation run.*

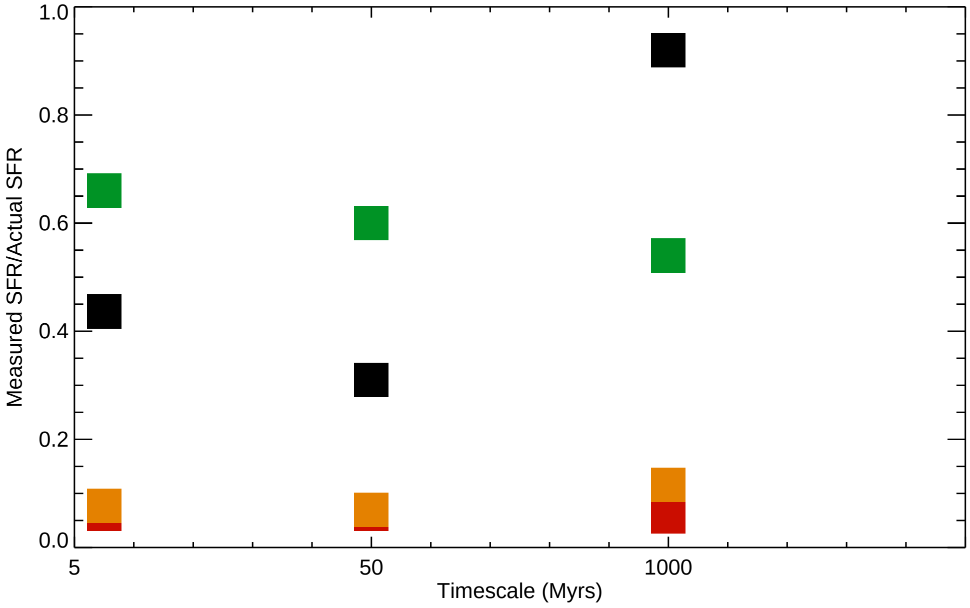

Figure 4.7 *Measured Hα SFRs versus actual SFRs integrated over various timescales.* Each color represents a different halo. Hα SFRs measured using the lineflux from the simulated SED. The measured SFRs come directly from the simulations, integrated over the timescale shown on the x-axis. This plot, although inconclusive, shows that the SFR does change as a function of timescale it's integrated over, although no single timescale appears to match with the Hα SFRs in this mass range.

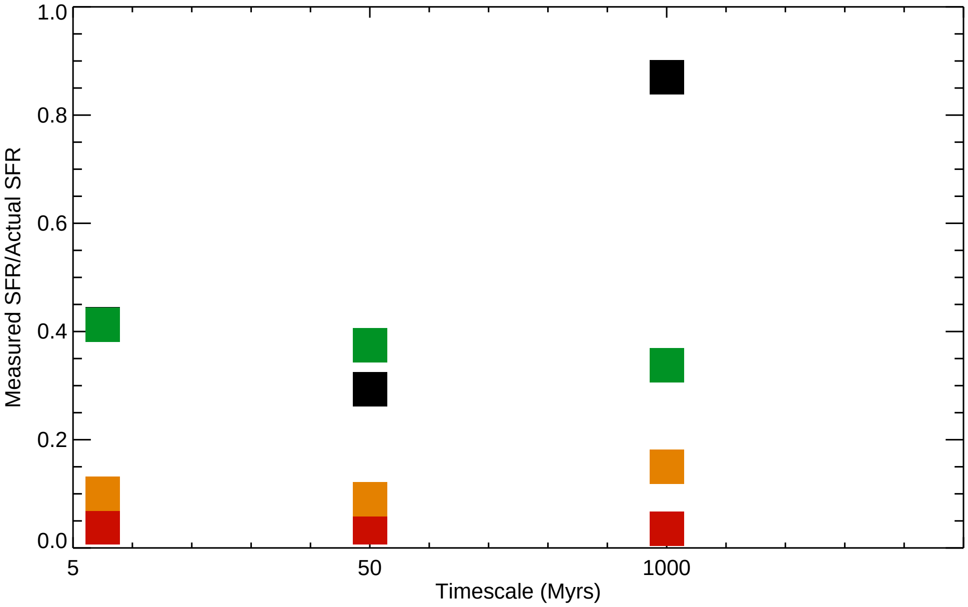

Figure 4.8 *Measured UV continuum SFRs versus actual SFRs integrated over various timescales.* Each color represents a different halo. Hα SFRs measured using the lineflux from the simulated SED. The measured SFRs come directly from the simulations, integrated over the timescale shown on the x-axis. This plot, although inconclusive, shows that the SFR does change as a function of timescale it's integrated over, although no single timescale appears to match with the UV SFRs in this mass range.

Chapter 5

CONCLUSIONS AND FUTURE WORK

5.1 Conclusions

This thesis broadly encompasses the complex topic of star formation, specifically in N-body+SPH cosmological simulations. Specifically this thesis is a step toward answering the following questions:

How do galaxies populate their dark matter halos? What affect does feedback and baryonic physics have on the stellar to halo mass relationship?

We measured the SHM (stellar mass – halo mass) relation for a set of simulated field galaxies and compared it with the redshift zero predictions based on data from the SDSS and the Abundance Matching Technique described in M12. We find very good agreement in normalization and shape over five orders of magnitude in stellar mass with the abundance matching result from M12. This agreement between simulations and observational data is due to two systematic factors: 1) An implementation of SF that relates the SF efficiency to the local H_2 abundance in resolved star forming regions, resulting in localized feedback that significantly lowers the SF efficiency and 2) "observing" the simulations to properly compare them to observational estimates of the SHM relation. Our analysis shows that adopting photometric stellar masses contributes to a 20-30% *systematic* reduction in the estimated stellar masses. Stellar mass estimates based on one band photometric magnitudes are likely to underestimate the contribution of old stellar populations (reflecting the larger contribution to the total flux coming from younger stars). This systematic effect is further exacerbated by the use of aperture based magnitudes, adding another 20-30% due to neglecting the contribution of low surface brightness populations. Finally, a third systematic effect comes from a difference in halo masses in collisionless (DM-only) simulations vs simulations including baryon physics and outflows. Baryon mass loss makes halo masses smaller by up to 30% when calculated at the same overdensity.

When and where are stars forming in galaxies? What is the structure of the ISM where these stars are forming? How does this relate to the underlying IMF of these systems?

We provide evidence that ISM pressure is redshift dependent by examining the ISM pressures during the formation of the present-day bulge and disk in 4 simulated disk galaxies. Because the present-day bulge predominantly forms early in the galaxy's history, it forms at higher pressures than the present-day disk. We show that in general, at early times, star formation occurs at higher pressures- specifically higher densities. We show that this is not the result of formation location and the higher densities found in the center of the protogalaxy: in general bulge and disk stars are forming over all formation radii. If ISM pressure and IMF are related as postulated in Krumholz (2011); Conroy & van Dokkum (2012), we have evidence for a redshift dependence of the IMF and further, that bulge stars formed with a different IMF from disk stars.

How well do observational star formation indicators trace star formation? What biases do we see when comparing simulations to observations? What does this tell us about the IMF in dwarf galaxies?

I show that our simulated galaxies have good agreement with the observed star formation rates derived from Hα and the FUV. I show that this agreement holds over an order of magnitude in resolution, and over two different ISM cooling subgrid models. I also looked at the variation in the measurement between z=0 and z=0.5 and find that over that timescale there is still good agreement between simulations and observations. In this section of my thesis, I showed the efficacy of utilizing SUNRISE to generate mock observations (images and SED) and utilizing these images to make measurements on the simulated galaxies. Now that the tools for implementing these measurements are built, I can answer questions about the variations in SFR derived from the two indicators discussed and trace their variation as a function of time over the course of a star formation burst. This ideally will address the question of what causes the variation: whether it soley is due to the bursty nature of dwarf star formation histories, or if the high mass end of the IMF is in fact different in these galaxies.

5.2 Future Work

Recent advances in imaging capabilities are now providing exquisite data on the study of high-redshift progenitors of today's massive galaxies. These high redshift galaxies are currently providing us with insights into the key mechanisms that shape the evolution of galaxies in the high mass regimes, placing constraints on current models of galaxy formation and evolution. In particular, the new near-infrared HST WFC3/IR imaging and spectroscopy provided by the Cosmic Assembly Near-IR Deep Extragalactic Legacy Survey (CANDELS) (Grogin et al., 2011; Koekemoer et al., 2011) and 3D-HST (van Dokkum et al., 2011), provide the necessary combination of depth, angular resolution and area to enable the most detailed and robust studies to date of rest-frame optical morphologies of galaxies at redshifts of $1 < z < 3$. In future work, I would like to run a series of cosmological hydrodynamic simulations at unprecedented high-resolution, that will resolve, down to 50 pc (2x better than the leading current simulations) scales, the ISM structure, star formation and physical structure of massive spirals. These simulations are key for the interpretation of recent observational results from CANDELS and 3D-HST that challenge the simple merger-driven picture of galaxy growth and evolution currently in favor. Our simulations already are able to produce galaxies with realistic present-day properties: including but not limited to morphology, stellar masses and baryon fractions (Munshi et al., 2013b; Governato et al., 2009, 2010). This new, state of the art suite of simulations will answer the following key questions:

- When and how do bulges assemble, acquire their mass and evolve in size?
- Given the present day morphology of a massive disk galaxy, when and where did the stars form in each component, as a function of time?

- How are star formation, assembly history and ISM structure related in massive disk galaxies?

In short, the implemenation and analysis of the simulations will provide critical observation-driven constraints to theoretical models of bulge and disk growth including the transition between bulge and disk dominated systems, and explain the relationship between star formation in progenitors of massive bulges and the underlying ISM and IMF.

HST high resolution data from WFC3 can provide the detailed morphology of high–z massive galaxies (Schawinski et al., 2011; Bundy et al., 2005). These high–z data have resolution comparable to or better than the *local* data from the Sloan Digital Sky Survey (SDSS). My future work will help interpret results from CANDELS and 3-D HST, which are providing a detailed census of massive galaxies at redshifts $1 < z < 3$. 3-D HST is a near-infrared spectroscopic survey designed to study the physical processes that shape galaxies in the distant universe. This survey provides rest-frame optical spectra for essentially every object in the field and is optimized to study galaxy formation within $1 < z < 3$. Its science objectives specifically address resolving the growth of disks and bulges, spacially and spectrally in addition to disentangling the processes that regulate star formation in massive galaxies. CANDELS, a complement to 3D-HST, uses HST to obtain deep images of more than $250,000$ galaxies with WFC3/IR and ACS imaging, over many fields imaged with other instruments. One of its key objectives is to study the "cosmic noon" and use these rest-frame optical observations to provide solid estimates of bulge and disk growth. Clearly, one of the key goals of both the CANDELS and 3D-HST surveys includes using rest-frame optical observations and spectroscopy at $1 < z < 3$ to provide solid estimates of bulge and disk growth and formation. Both surveys allow astronomers, for the *first time* to directly study high redshift morphologies of galaxies.

Published data from these surveys, empirically explore the evolutionary factors that lead to a lack of star formation in massive galaxies and find evidence for dramatic changes in the morphologies of massive galaxies with redshift, specifically at $z \sim 2$, marking a key transition from being disk to bulge dominated (Bell et al., 2012; Bruce et al., 2012). Additionally, while most of the quiescent galaxies are bulge-dominated, the data indicate that a significant fraction of quiescent galaxies in this redshift range, still have disk-dominated morphologies. Furthermore, these data highlight that bulges are more compact with increasing z, although there is no significant mass evolution (Bruce et al. 2012).

Additionally, recent observational and theoretical work (Conroy & van Dokkum, 2012; Krumholz, 2011) indicate that in spheroidal, high mass systems (i.e., high velocity dispersion systems), stars are forming in a higher pressure ISM when compared to stars formed in other systems. The higher pressure ISM correlates with the initial mass function (IMF)- in fact, higher pressures indicate a more bottom heavy IMF. It is suggested in Conroy and VanDokkum (2012) that this IMF variation is correlated, not only with the pressure of formation, but additionally with the intensity of star formation: higher SFR densities and higher pressures correspond to a more bottom heavy IMF. This project will provide critical theoretical constraints to the above results from the CANDELS and 3D-HST surveys by directly tracing the formation of bulge and disk components of massive galaxies in high resolution simulations. As a result, this work will *directly* address the observers' key goal of understanding bulge and disk growth and subsequent evolution, in massive spirals.

The above observational evidence challenges theoretical models to: (1) include a mode in which star formation quenching is not connected to morphological transformation, (2) explain the relationship between active and passive disks and, (3) predict the rapid demise of star forming disks and the slow emergence of bulge-dominated morphologies. Theoretical evidence points out that the simple therory of merger driven assembly of bulges (Hopkins et al., 2005; Oser et al., 2012), is likely incomplete and and too simplistic. Rather, HST data point to an early growth of a compact bulge and subsequent size evolution in later epochs. The high-z evidence is in apparent contrast with the low-z size-mass relationship for galaxy spheroids suggesting that secular processes outside of merging may be responsible for morphology evolution.

As stated above, I will focus on very high resolution 'zoomed-in' simulations in a ΛCDM Universe. These simulations will naturally include mergers, feedback, cold flows and cooling of shock heated gas (Kereš et al., 2009; Brooks et al., 2009; Dekel et al., 2009) in a cosmological setting and will provide a detailed approach to the growth of spheroids and disks *over the whole Hubble time*.

ChaNGa: An NBody+SPH code with star formation linked to H_2 and SN and SMBH Feedback.

GASOLINE, our parallel SPH code, has received two major updates: Collaborator Wadsley has introduced a new SPH implementation (Hopkins, 2013) that successfully models Kelvin-Helmholtz instabilities and passes all the tests outlined in Agertz et al. (2007). This makes upgraded GASOLINE, now called ChaNGa, competitive with the new proposed grid codes, while keeping the versatility and simplicity of its Lagrangian approach. Quinn and collaborators have adapted ChaNGa to an advanced parallel run-time system with a dynamic load balancing scheme (CHARM++) to scale efficiently up to housands of CPUs and enable efficient use of heterogeneous architectures. Advantages of this new code include:

- a *new* SPH treatment of hydrodynamics and diffusion processes
- Scaling up to several thousands of CPUs- allowing simulations to run faster and more efficiently.
- Star Formation with different IMFs, O and Fe metal enrichment.
- Gas heating from SN feedback, SMBHs and a cosmic UV background including QSOs.
- H_2 shielding and metal line cooling; SF related to the local abundance of H_2.

How can numerical simulations address the above questions?

The key questions I hope to address can now be directly tackled by numerical simulations in a full cosmological setting. Our understanding of the formation of galaxy bulges and disks and the quality of hydrodynamical methods has greatly improved in the past few years, since simulations are now able to resolve scales $\sim 5\%$ of the typical disk scale length and conserve the angular momentum of infalling gas (Robertson et al., 2004; Brooks et al., 2011; Keres et al., 2011). Recent work has highlighted the role of feedback (from SN and BHs) and has demonstrated that galaxy outflows are efficient at removing baryons and possibly self–regulate the growth of galaxies and their stellar masses (Arav et al., 2008; Bouché et al., 2012; Governato et al., 2010; Di Matteo et al., 2005; Oppenheimer et al., 2010; Choi & Nagamine, 2011; Munshi et al., 2013b). Simulations coupled with analytical modeling of processes at unresolved scales can now achieve the dynamical range and physical detail necessary to follow the assembly of massive disk galaxies and the their corresponding components over a Hubble time. These high resolution simulations can now reliably predict morphological evolution and take CANDELS observations as model constraints.

Because of this vast improvement in hydrodynamical models, I can use my proposed simulations to *directly* address the proposal's key questions:

When and how do bulges assemble, acquire their mass and evolve in size? Given the present day morphology of a massive disk galaxy, when and where did the stars form in each component, as a function of time?:

Using a dynamical decomposition based on energy and angular momentum, I can decompose each of the simulated galaxies into its structural components: bulge, disk and halo. I will do this from $z = 0$ *to* $z = 3$ *and follow where the stars that form each structural component come from, as a function of time, in order to understand the assembly history of the bulge, including utilizing full merger trees for each of the simulations.*

How are star formation, assembly history and ISM structure related in massive disk galaxies?: Is there a connection between ISM pressure, merger history, and assembly history and the underlying IMF in the components of these galaxies (Krumholz, 2011; Conroy & van Dokkum, 2012)? My results (Munshi et al., 2013a) indicate that the structure of the ISM when the bulge stars formed is different than that of the ISM when disk stars formed, possibly supporting observational evidence for a varying IMF. What remains to be answered is *what* actually causes this variation: what in the history of these galaxies leads to this pressure differential? *I have already developped the software to trace stars back* *to the ISM in which they formed and can apply this software to the new, much more massive simulations. Coupled with the analysis of how each component forms, in addition to generating full merger trees, I can trace how and why the star forming ISM varies, what causes the variation in ISM pressures and potentially isolate which process drives a time-dependent IMF.*

BIBLIOGRAPHY

Abadi, M. G., Navarro, J. F., Steinmetz, M., & Eke, V. R. 2003, ApJ, 591, 499

Agertz, O. et al. 2007, MNRAS, 380, 963

Arav, N., Moe, M., Costantini, E., Korista, K. T., Benn, C., & Ellison, S. 2008, ApJ, 681, 954

Avila-Reese, V., Colín, P., González-Samaniego, A., Valenzuela, O., Firmani, C., Velázquez, H., & Ceverino, D. 2011, ApJ, 736, 134

Barnes, J., & Efstathiou, G. 1987, ApJ, 319, 575

Bastian, N., Covey, K. R., & Meyer, M. R. 2010, ARA&A, 48, 339

Behroozi, P. S., Conroy, C., & Wechsler, R. H. 2010, ApJ, 717, 379

Behroozi, P. S., Wechsler, R. H., & Conroy, C. 2013, ApJ, 770, 57

Bell, E. F., & de Jong, R. S. 2001, ApJ, 550, 212

Bell, E. F., & Kennicutt, Jr., R. C. 2001, ApJ, 548, 681

Bell, E. F., McIntosh, D. H., Katz, N., & Weinberg, M. D. 2003, ApJS, 149, 289

Bell, E. F. et al. 2012, ApJ, 753, 167

Benson, A. J. 2010, 495, 33

Benson, A. J., Frenk, C. S., Lacey, C. G., Baugh, C. M., & Cole, S. 2002, MNRAS, 333, 177

Bigiel, F., Leroy, A., Walter, F., Brinks, E., de Blok, W. J. G., Madore, B., & Thornley, M. D. 2008, AJ, 136, 2846

Binney, J., Gerhard, O., & Silk, J. 2001, MNRAS, 321, 471

Blain, A. W., Chapman, S. C., Smail, I., & Ivison, R. 2004, ApJ, 611, 725

Blanton, M. R. et al. 2001, AJ, 121, 2358

Blumenthal, G. R., Faber, S. M., Primack, J. R., & Rees, M. J. 1984, Nature, 311, 517

Bode, P., Ostriker, J. P., & Turok, N. 2001, ApJ, 556, 93

Bouché, N., Hohensee, W., Vargas, R., Kacprzak, G. G., Martin, C. L., Cooke, J., & Churchill, C. W. 2012, MNRAS, 426, 801

Bower, R. G., Benson, A. J., & Crain, R. A. 2012, MNRAS, 422, 2816

Bower, R. G., Benson, A. J., Malbon, R., Helly, J. C., Frenk, C. S., Baugh, C. M., Cole, S., & Lacey, C. G. 2006, MNRAS, 370, 645

Bower, R. G., Vernon, I., Goldstein, M., Benson, A. J., Lacey, C. G., Baugh, C. M., Cole, S., & Frenk, C. S. 2010, MNRAS, 407, 2017

Boylan-Kolchin, M., Bullock, J. S., & Kaplinghat, M. 2011a, ArXiv e-prints

—. 2011b, MNRAS, 415, L40

Boylan-Kolchin, M., Springel, V., White, S. D. M., Jenkins, A., & Lemson, G. 2009, MNRAS, 398, 1150

Brook, C. B. et al. 2011, MNRAS, 415, 1051

Brook, C. B., Stinson, G., Gibson, B. K., Wadsley, J., & Quinn, T. 2012, MNRAS, 424, 1275

Brooks, A. M., Governato, F., Booth, C. M., Willman, B., Gardner, J. P., Wadsley, J., Stinson, G., & Quinn, T. 2007, ApJ, 655, L17

Brooks, A. M., Governato, F., Quinn, T., Brook, C. B., & Wadsley, J. 2009, ApJ, 694, 396

Brooks, A. M. et al. 2011, ApJ, 728, 51

Brooks, A. M., & Zolotov, A. 2012, ArXiv e-prints

Bruce, V. A. et al. 2012, MNRAS, 427, 1666

Buat, V. 1992, A&A, 264, 444

Buat, V., Donas, J., & Deharveng, J. M. 1987, A&A, 185, 33

Bullock, J. S., Kolatt, T. S., Sigad, Y., Somerville, R. S., Kravtsov, A. V., Klypin, A. A., Primack, J. R., & Dekel, A. 2001, MNRAS, 321, 559

Bundy, K., Ellis, R., & Conselice, C. 2005, astro–ph/0502204

Burkert, A. 1995, ApJ, 447, L25

Cannon, J. M. et al. 2011, ApJ, 739, L22

Cappellari, M. et al. 2012, Nature, 484, 485

Ceverino, D., & Klypin, A. 2009, ApJ, 695, 292

Chabrier, G. 2003, PASP, 115, 763

Choi, J.-H., & Nagamine, K. 2011, MNRAS, 410, 2579

Christensen, C., Governato, F., Quinn, T., Brooks, A. M., Fisher, D. B., Shen, S., McCleary, J., & Wadsley, J. 2012a, ArXiv e-prints

—. 2012b, ArXiv e-prints

Christensen, C., Quinn, T., Governato, F., Stilp, A., Shen, S., & Wadsley, J. 2012c, MNRAS, 425, 3058

—. 2012d, MNRAS, 425, 3058

Cloet-Osselaer, A., De Rijcke, S., Schroyen, J., & Dury, V. 2012, MNRAS, 2952

Colín, P., Avila-Reese, V., Vázquez-Semadeni, E., Valenzuela, O., & Ceverino, D. 2010, ApJ, 713, 535

Conroy, C., & van Dokkum, P. G. 2012, ApJ, 760, 71

Conroy, C., Wechsler, R. H., & Kravtsov, A. V. 2006, ApJ, 647, 201

Croton, D. J. 2009, MNRAS, 394, 1109

Dalcanton, J. J. 1998, ApJ, 495, 251

Davis, M., Efstathiou, G., Frenk, C. S., & White, S. D. M. 1985, ApJ, 292, 371

de Souza, R. S., Rodrigues, L. F. S., Ishida, E. E. O., & Opher, R. 2011, MNRAS, 415, 2969

Dekel, A. et al. 2009, Nature, 457, 451

Dekel, A., & Silk, J. 1986, ApJ, 303, 39

Di Matteo, T., Springel, V., & Hernquist, L. 2005, Nature, 433, 604

Dutton, A. A., Macciò, A. V., Mendel, J. T., & Simard, L. 2013, MNRAS, 432, 2496

Eke, V. R., Navarro, J. F., & Steinmetz, M. 2001, ApJ, 554, 114

Fakhouri, O., Ma, C.-P., & Boylan-Kolchin, M. 2010, MNRAS, 406, 2267

Fall, S. M., & Efstathiou, G. 1980, MNRAS, 193, 189

Ferland, G. J., Korista, K. T., Verner, D. A., Ferguson, J. W., Kingdon, J. B., & Verner, E. M. 1998a, PASP, 110, 761

—. 1998b, PASP, 110, 761

Frenk, C. S., White, S. D. M., Efstathiou, G., & Davis, M. 1985, Nature, 317, 595

Geha, M., Blanton, M. R., Masjedi, M., & West, A. A. 2006, ApJ, 653, 240

Geller, M. J., Diaferio, A., Kurtz, M. J., Dell'Antonio, I. P., & Fabricant, D. G. 2012, AJ, 143, 102

Genel, S., Vogelsberger, M., Nelson, D., Sijacki, D., Springel, V., & Hernquist, L. 2013, MNRAS

Genzel, R. et al. 2012, ApJ, 746, 69

Gill, S. P. D., Knebe, A., & Gibson, B. K. 2004, MNRAS, 351, 399

Gilmore, G., Hernandez, X., & Valls-Gabaud, D. 2000, Ap&SS, 272, 61

Giovanelli, R. et al. 2005, AJ, 130, 2598

Gnedin, N. Y. 2000, ApJ, 542, 535

Gnedin, N. Y., Tassis, K., & Kravtsov, A. V. 2009, ApJ, 697, 55

Governato, F. et al. 2010, Nature, 463, 203

—. 2009, MNRAS, 398, 312

Governato, F., Willman, B., Mayer, L., Brooks, A., Stinson, G., Valenzuela, O., Wadsley, J., & Quinn, T. 2007, MNRAS, 374, 1479

Governato, F. et al. 2012, MNRAS, 422, 1231

Graham, A. W., Driver, S. P., Petrosian, V., Conselice, C. J., Bershady, M. A., Crawford, S. M., & Goto, T. 2005, AJ, 130, 1535

Grogin, N. A. et al. 2011, ApJS, 197, 35

Guedes, J., Callegari, S., Madau, P., & Mayer, L. 2011, ApJ, 742, 76

Guo, Q., White, S., Li, C., & Boylan-Kolchin, M. 2010, MNRAS, 404, 1111

Haardt, F., & Madau, P. 1996, ApJ, 461, 20

Heavens, A., Panter, B., Jimenez, R., & Dunlop, J. 2004, Nature, 428, 625

Hennebelle, P., & Chabrier, G. 2008, ApJ, 684, 395

Hopkins, A. M., McClure-Griffiths, N. M., & Gaensler, B. M. 2008, ApJ, 682, L13

Hopkins, P. F. 2012a, MNRAS, 423, 2016

—. 2012b, MNRAS, 423, 2037

—. 2013, MNRAS, 433, 170

Hopkins, P. F., Hernquist, L., Cox, T. J., Di Matteo, T., Martini, P., Robertson, B., & Springel, V. 2005, ApJ, 630, 705

Hopkins, P. F., Keres, D., Murray, N., Quataert, E., & Hernquist, L. 2011a, ArXiv e-prints

Hopkins, P. F., Quataert, E., & Murray, N. 2011b, ArXiv e-prints

Hopkins, P. F. et al. 2009, MNRAS, 397, 802

Huang, S., Haynes, M. P., Giovanelli, R., Brinchmann, J., Stierwalt, S., & Neff, S. G. 2012, ArXiv e-prints

Jenkins, A. et al. 1998, ApJ, 499, 20

Johansson, P. H., Naab, T., & Ostriker, J. P. 2012, ApJ, 754, 115

Jonsson, P. 2006, MNRAS, 372, 2

Jonsson, P., Groves, B. A., & Cox, T. J. 2010, MNRAS, 403, 17

Katz, N. 1992, ApJ, 391, 502

Katz, N., & White, S. D. M. 1993, ApJ, 412, 455

Kauffmann, G. et al. 2003, MNRAS, 341, 33

Kaufmann, D. E. 1993, PhD thesis, Florida University

Keres, D., Vogelsberger, M., Sijacki, D., Springel, V., & Hernquist, L. 2011, ArXiv e-prints

Kereš, D., Katz, N., Davé, R., Fardal, M., & Weinberg, D. H. 2009, MNRAS, 396, 2332

Klypin, A., Kravtsov, A. V., Valenzuela, O., & Prada, F. 1999, ApJ, 522, 82

Knollmann, S. R., & Knebe, A. 2009, ApJS, 182, 608

Koekemoer, A. M. et al. 2011, ApJS, 197, 36

Kormendy, J., & Sanders, D. B. 1992, ApJ, 390, L53

Kroupa, P., & Weidner, C. 2003, ApJ, 598, 1076

Krumholz, M. R. 2011, ApJ, 743, 110

Krumholz, M. R., McKee, C. F., & Tumlinson, J. 2009, ApJ, 699, 850

Kuhlen, M., Diemand, J., Madau, P., & Zemp, M. 2008, Journal of Physics Conference Series, 125, 012008

Kuhlen, M., Krumholz, M., Madau, P., Smith, B., & Wise, J. 2011, ArXiv e-prints

Lada, C. J., & Lada, E. A. 2003, ARA&A, 41, 57

Larson, R. B. 2005, MNRAS, 359, 211

Leauthaud, A. et al. 2011, ArXiv e-prints

—. 2012, ApJ, 744, 159

Leitherer, C. et al. 1999, ApJS, 123, 3

Leitner, S. N. 2012, ApJ, 745, 149

Macciò, A. V., Stinson, G., Brook, C. B., Wadsley, J., Couchman, H. M. P., Shen, S., Gibson, B. K., & Quinn, T. 2012, ApJ, 744, L9

Madau, P., Diemand, J., & Kuhlen, M. 2008, ApJ, 679, 1260

Mandelbaum, R., Seljak, U., Kauffmann, G., Hirata, C. M., & Brinkmann, J. 2006, MNRAS, 368, 715

Maraston, C. et al. 2012, ArXiv e-prints

Martin, C. L. 1999, ApJ, 513, 156

Mashchenko, S., Couchman, H. M. P., & Wadsley, J. 2006, Nature, 442, 539

Mateo, M. L. 1998, ARA&A, 36, 435

McCarthy, I. G., Schaye, J., Bower, R. G., Ponman, T. J., Booth, C. M., Dalla Vecchia, C., & Springel, V. 2011, MNRAS, 412, 1965

McCarthy, I. G., Schaye, J., Font, A. S., Theuns, T., Frenk, C. S., Crain, R. A., & Dalla Vecchia, C. 2012, ArXiv e-prints

Mo, H. J., Mao, S., & White, S. D. M. 1998, MNRAS, 295, 319

Moore, B. 1994, Nature, 370, 629

Moore, B., Governato, F., Quinn, T., Stadel, J., & Lake, G. 1998, ApJ, 499, L5+

Moore, B., Quinn, T., Governato, F., Stadel, J., & Lake, G. 1999a, MNRAS, 310, 1147

—. 1999b, MNRAS, 310, 1147

More, S., van den Bosch, F. C., & Cacciato, M. 2009, MNRAS, 392, 917

Moster, B. P., Naab, T., & White, S. D. M. 2012, ArXiv e-prints

Moster, B. P., Somerville, R. S., Maulbetsch, C., van den Bosch, F. C., Macciò, A. V., Naab, T., & Oser, L. 2010, ApJ, 710, 903

Munshi, F., Christensen, C., Quinn, T. R., Governato, F., Wadsley, J., Loebman, S., & Shen, S. 2013a, ArXiv e-prints

Munshi, F. et al. 2013b, ApJ, 766, 56

Narayanan, D., & Davé, R. 2012, MNRAS, 423, 3601

Narayanan, D., & Hopkins, P. F. 2013, MNRAS, 433, 1223

Nickerson, S., Stinson, G., Couchman, H. M. P., Bailin, J., & Wadsley, J. 2011, MNRAS, 415, 257

Ogiya, G., & Mori, M. 2012, ArXiv e-prints

Oh, S.-H., Brook, C., Governato, F., Brinks, E., Mayer, L., de Blok, W. J. G., Brooks, A., & Walter, F. 2011a, AJ, 142, 24

—. 2011b, AJ, 142, 24

Okamoto, T., Gao, L., & Theuns, T. 2008, MNRAS, 390, 920

Oppenheimer, B. D., Davé, R., Kereš, D., Fardal, M., Katz, N., Kollmeier, J. A., & Weinberg, D. H. 2010, MNRAS, 406, 2325

Oser, L., Naab, T., Ostriker, J. P., & Johansson, P. H. 2012, ApJ, 744, 63

Padoan, P., Haugbølle, T., & Nordlund, Å. 2012, ApJ, 759, L27

Padoan, P., Nordlund, A., & Jones, B. J. T. 1997, MNRAS, 288, 145

Panter, B., Heavens, A. F., & Jimenez, R. 2004, MNRAS, 355, 764

Pasetto, S., Grebel, E. K., Berczik, P., Spurzem, R., & Dehnen, W. 2010, A&A, 514, A47

Pforr, J., Maraston, C., & Tonini, C. 2012, ArXiv e-prints

Piontek, F., & Steinmetz, M. 2011, MNRAS, 410, 2625

Pontzen, A., & Governato, F. 2012a, ArXiv e-prints

—. 2012b, MNRAS, 421, 3464

Pontzen, A. et al. 2008, MNRAS, 390, 1349

Quinn, T., Katz, N., & Efstathiou, G. 1996, MNRAS, 278, L49

Reddick, R. M., Wechsler, R. H., Tinker, J. L., & Behroozi, P. S. 2012, ArXiv e-prints

Reed, D., Gardner, J., Quinn, T., Stadel, J., Fardal, M., Lake, G., & Governato, F. 2003, MNRAS, 346, 565

Reed, D. S., Governato, F., Quinn, T., Stadel, J., & Lake, G. 2007, MNRAS, 378, 777

Reid, B. A. et al. 2010, MNRAS, 404, 60

Robertson, B., Yoshida, N., Springel, V., & Hernquist, L. 2004, ApJ, 606, 32

Sales, L. V., Navarro, J. F., Theuns, T., Schaye, J., White, S. D. M., Frenk, C. S., Crain, R. A., & Dalla Vecchia, C. 2012, MNRAS, 3041

Salim, S. et al. 2007, ApJS, 173, 267

Santini, P. et al. 2012, A&A, 538, A33

Sawala, T., Frenk, C. S., Crain, R. A., Jenkins, A., Schaye, J., Theuns, T., & Zavala, J. 2012, ArXiv e-prints

Sawala, T., Guo, Q., Scannapieco, C., Jenkins, A., & White, S. 2011, MNRAS, 413, 659

Scannapieco, C., Gadotti, D. A., Jonsson, P., & White, S. D. M. 2010, MNRAS, 407, L41

Scannapieco, C. et al. 2012, MNRAS, 423, 1726

Scannapieco, C., White, S. D. M., Springel, V., & Tissera, P. B. 2011, MNRAS, 417, 154

Schawinski, K., Treister, E., Urry, C. M., Cardamone, C. N., Simmons, B., & Yi, S. K. 2011, ApJ, 727, L31+

Shen, S., Wadsley, J., & Stinson, G. 2010, MNRAS, 407, 1581

Sheth, R. K., Mo, H. J., & Tormen, G. 2001, MNRAS, 323, 1

Shimasaku, K. et al. 2001, AJ, 122, 1238

Sijacki, D., Springel, V., Di Matteo, T., & Hernquist, L. 2007, MNRAS, 380, 877

Somerville, R. S., Hopkins, P. F., Cox, T. J., Robertson, B. E., & Hernquist, L. 2008, MNRAS, 391, 481

Somerville, R. S., & Primack, J. R. 1999, MNRAS, 310, 1087

Springel, V., Di Matteo, T., & Hernquist, L. 2005a, MNRAS, 361, 776

Springel, V., & Hernquist, L. 2003, MNRAS, 339, 312

Springel, V. et al. 2008, Nature, 456, 73

—. 2005b, Nature, 435, 629

Stinson, G., Brook, C., Macciò, A. V., Wadsley, J., Quinn, T. R., & Couchman, H. M. P. 2012, ArXiv e-prints

Stinson, G., Seth, A., Katz, N., Wadsley, J., Governato, F., & Quinn, T. 2006, MNRAS, 373, 1074

Teyssier, R. et al. 2009, A&A, 497, 335

Teyssier, R., Pontzen, A., Dubois, Y., & Read, J. 2012, ArXiv e-prints

Thacker, R. J., & Couchman, H. M. P. 2000, ApJ, 545, 728

Toomre, A., & Toomre, J. 1972, ApJ, 178, 623

Treu, T., Auger, M. W., Koopmans, L. V. E., Gavazzi, R., Marshall, P. J., & Bolton, A. S. 2010, ApJ, 709, 1195

Trujillo-Gomez, S., Klypin, A., Primack, J., & Romanowsky, A. J. 2011, ApJ, 742, 16

Vale, A., & Ostriker, J. P. 2004, MNRAS, 353, 189 van Daalen, M. P., Angulo, R. E., & White, S. D. M. 2012, ArXiv e-prints

van Dokkum, P. G. et al. 2011, ApJ, 743, L15

van Dokkum, P. G., & Conroy, C. 2011, ApJ, 735, L13

Vázquez, G. A., & Leitherer, C. 2005, ApJ, 621, 695

Wadsley, J. W., Stadel, J., & Quinn, T. 2004, New Astronomy, 9, 137

Wang, J., & White, S. D. M. 2009, MNRAS, 396, 709

Wang, P., Li, Z., Abel, T., & Nakamura, F. 2010, ApJ, 709, 27

Warren, B. E., Jerjen, H., & Koribalski, B. S. 2006a, AJ, 131, 2056

—. 2006b, AJ, 131, 2056

Weidner, C., Ferreras, I., Vazdekis, A., & La Barbera, F. 2013, MNRAS, 435, 2274

Weisz, D. R. et al. 2012, ApJ, 744, 44

White, S. D. M., Davis, M., Efstathiou, G., & Frenk, C. S. 1987, Nature, 330, 451

White, S. D. M., & Frenk, C. S. 1991, ApJ, 379, 52

White, S. D. M., & Rees, M. J. 1978, MNRAS, 183, 341

Willman, B. et al. 2005, ApJ, 626, L85

Willman, B., Governato, F., Dalcanton, J. J., Reed, D., & Quinn, T. 2004, MNRAS, 353, 639

Wise, J. H., Abel, T., Turk, M. J., Norman, M. L., & Smith, B. D. 2012a, ArXiv e-prints

Wise, J. H., Turk, M. J., Norman, M. L., & Abel, T. 2012b, ApJ, 745, 50

Yang, X., Mo, H. J., van den Bosch, F. C., Zhang, Y., & Han, J. 2012, ApJ, 752, 41

Yasuda, N. et al. 2001, AJ, 122, 1104

Zheng, Z., Coil, A. L., & Zehavi, I. 2007, ApJ, 667, 760

Zolotov, A. et al. 2012, ApJ, 761, 71

VITA

Ferah Munshi began her study of Astronomy after her third year at the University of California, Berkeley under the supervision of Professor Saul Permlmutter and Dr. Andrew West. After graduating with a Bachelor of Arts from Berkeley in 2008, she made her way to the University of Washington to begin the graduate program in the Astronomy Department. She completed her doctorate at the University of Washington in December 2013.